Check for updates

Fire and Materials

WILEY

RESEARCH ARTICLE OPEN ACCESS

Exploratory Simulations on the Effectiveness of Sand Protection Strategies Against Firebrand Accumulation in Wildfires

Simona Dossi[1,2] | Wojciech Węgrzyński[3] | Guillermo Rein[1]

[1]Department of Mechanical Engineering, and Leverhulme Centre for Wildfires, Environment, and Society, Imperial College London, London, UK | [2]Department of Chemical Engineering, Centre for Technological Risk Studies (CERTEC), Universitat Politècnica de Catalunya Barcelona Tech, Barcelona, Spain | [3]Instytut Techniki Budowlanej (ITB), Warszawa, Poland

Correspondence: Guillermo Rein (g.rein@imperial.ac.uk)

Received: 30 September 2024 | **Revised:** 30 January 2025 | **Accepted:** 2 February 2025

Funding: This project has received funding from the European Union's Horizon 2020 research and innovation programme under the Marie Skłodowska-Curie grant agreement No. 860787, as part of the Pyrolife ITN.

Keywords: FDS | firebrand | protection | sand | wildfires

ABSTRACT

Firebrands are the leading cause of infrastructure damage during wildfires. However, dedicated protections specifically designed to mitigate firebrand accumulation, remain limited. In contrast, infrastructure protection strategies against sand accumulation have been developed, implemented and studied in detail. Because both sand and firebrands are airborne particles, this paper explores the potential applicability of sand protection strategies to mitigate firebrand exposure. A literature review of existing protection strategies from both sand and firebrands is presented, followed by exploratory numerical simulations using Fire Dynamics Simulator (FDS). The simulations study the effectiveness of shielding a simplified cubic structure from particles simulating firebrand exposure under varying ambient wind speeds (4, 6, and 8 m/s). Two sand protection strategies are simulated, a trench and wall protection; results indicate the selected protections have the potential to reduce firebrand exposure to a target obstacle. The findings provide novel insights into the feasibility of translating sand protection strategies to firebrand mitigation and establish a foundation for innovative infrastructure solutions against wildfires.

1 | Introduction

1.1 | Wildfire Firebrand Exposure

Highly destructive wildfires have caused significant social, infrastructure, and economic losses in recent years; wildfire-caused damage and associate costs are expected to increase in future years [1]. Firebrands are airborne particles of burning fuel, generated during fire events, which contribute to rapid wildfire spread by igniting discontinuous spot fires upon landing [2]. Firebrands are regularly reported as the leading cause of wildland urban-interface (WUI) infrastructure ignition and damage [3–5]; attributed to as high as > 90% of building wildfire ignitions in urban areas [6]. Structural ignition by firebrands can occur directly, through firebrand accumulation on the exterior envelope or entry into structure openings (e.g., open windows, vents, and chimneys) [7, 8], or indirectly through firebrand ignition of nearby fuel and subsequent flaming exposure [9]. Wildfire firebrand spotting dynamics have been investigated on a landscape scale [10, 11], full building structure scale [9, 12], and building component scale [13], both computationally and experimentally. This paper considers building-scale firebrand exposure computationally, specifically by exploring the possible protection strategies applications of sand accumulation infrastructure protection. We introduce the similarities between sand exposure and firebrand exposure towards building, and

This is an open access article under the terms of the Creative Commons Attribution License, which permits use, distribution and reproduction in any medium, provided the original work is properly cited.

© 2025 The Author(s). *Fire and Materials* published by John Wiley & Sons Ltd.

explore whether the developed sand-shielding infrastructure protection strategies may be applicable and promising in firebrand protection of buildings.

FDS has been applied in literature to investigate firebrand transport and deposition. Wadhwani et al. [14] verified the FDS Lagrangian spherical drag model with laboratory tests comparing cubiform and cylindrical, non-combusting firebrands' short-range trajectories. Results indicate FDS underestimates landing distance with an acceptable error; a higher discrepancy is recorded for cylindrical particles compared to cubiform particles due to non-uniform drag effects neglected by FDS [14]. Mankame and Shotorban [15] modified the Lagrangian tracking model within the FDS framework by including both translational and rotational particle motion and adding a mass loss rate model considering pyrolysis and charring firebrand mass change to particles assumed to be thermally thin [15]. This modified model was used to analyse firebrand particle deposition patterns around a cubic obstacle, along with a parametric study varying dimensions of the cubic structure. FDS has also been applied to support the analysis of firebrand accumulation experimental investigations; Suzuki and Manzello [16, 17] modelled the flow characteristics within the wind tunnel used for investigations of firebrand accumulation patterns around obstacles under varying wind conditions [16, 17]. Suzuki and Manzello present an analytical approach considering the drag and friction forces acting on firebrand particles to estimate the local flow speed threshold for firebrand accumulation to occur; FDS is applied to identify the locations of this flow threshold throughout the wind tunnel domain.

Wickramasinghe et al. [18] use FDS to conduct an inverse analysis, based on firebrand generation experimental and prescribed burn investigations results, to estimate the firebrand generation rate for a single tree ($3.22\,\text{pcs}\,\text{MW}^{-1}\,\text{s}^{-1}$) and a forested land ($4.18\,\text{pcs}\,\text{MW}^{-1}\,\text{s}^{-1}$); the analysis was extended to quantify effects of vegetation type (considering Douglas fit, Grand fir, Ponderosa Pine, and Western Juniper), wind speed and fuel moisture content on firebrand generation flux [18]. Wickramasinghe et al. [12] used FDS simulations to model different wildfire conditions, corresponding to Fire Danger Index (FDI) rating of 100, 800, and 50, to quantify the relationship between radiative heat flux and firebrand flux on structures; results found a logarithmic relationship correlating firebrand flux exposure and radiative heat flux [12]. Table 1 summarises relevant Lagrangian particle properties and computational domain and mesh grid dimensions for these FDS studies.

This work presents FDS simulations, in coherence with existing firebrand exposure studies using FDS, to investigate the applicability of firebrand protection strategies for infrastructures. A literature review is conducted to analyse the existing literature

TABLE 1 | Summary of relevant parameters applied in FDS computational literature studies investigating firebrand exposure.

Lagrangian particle properties	Mesh and domain dimensions	References
Six types of particles are introduced with densities of $\overline{\mu} \pm \sigma/4$, $\overline{\mu} \pm 3\sigma/4$, $\overline{\mu} \pm 3\sigma/2$, where: *Spherical particles*: Average length: 12.45 mm $\overline{\mu} = 428.3\,\text{kg/m}^3$ ($\sigma = 48.9\,\text{kg/m}^3$) *Cylindrical particles*: Average length: 11.6 mm Average diameter: 6.2 mm $\overline{\mu} = 492.9\,\text{kg/m}^3$ ($\sigma = 44.3\,\text{kg/m}^3$)	Domain size: 7 m × 1.2 m × 2 m Uniform mesh grid sizes: 10, 20, 40 and 40 mm, for 4 meshes in domain	[14]
Cylindrical particles: Initial length: 3 mm Initial diameter: 40 mm Initial density: $570\,\text{kg/m}^3$	Domain size: 0.8 m × 0.4 m × 0.4 m Uniform mesh grid size: 2.5 mm	[15]
For single tree simulation: *Cylindrical particles*: Mass range: [0.005 g, 2.00 g] 97% particles < 1.00 g 60% particles have length < 50 mm and diameter < 3.7 mm *For forest simulation*: *Cylindrical particles*: Details not provided.	Uniform mesh grid size: 50 mm *For single tree simulation*: Domain size: 8 m × 8 m × 10 m *For forest simulation*: Domain size: 336 m × 162 m × height m—different heights tested	[18]
Cubiform particles: Final density range: [$344\,\text{kg/m}^3$] *Cylindrical particles*: Final density range: [300–$380\,\text{kg/m}^3$] *Spherical particles*: Final density range: [295–$240\,\text{kg/m}^3$]	Uniform mesh grid sizes: 1.5, 0.75 m, for 2 meshes in domain. Domain size: 336 m × 100 m × 90 m	[12]

10991018, 2025, 5, Downloaded from https://onlinelibrary.wiley.com/doi/10.1002/fam.3286 by Imperial College London, Wiley Online Library on [07/07/2026]. See the Terms and Conditions (https://onlinelibrary.wiley.com/terms-and-conditions) on Wiley Online Library for rules of use; OA articles are governed by the applicable Creative Commons License

TABLE 2 | Research publications investigating wildfire firebrand hazard protection or mitigation strategies.

Protection method	Brief description	References
Vent screens	Experimental investigation of unconsidered characteristics influencing wire screens protection performance against firebrand entry. Results indicate screen porosity, screen type, and wind speed are significant influencing parameters for performance, while screen orientation is less influential on performance.	[25]
Full-house fire blanket	Takahashi tested building-scale fire blankets in the laboratory and in prescribed wildland fires exposures. By enclosing the full building in a fire blanket, firebrands are blocked from entering and accumulating on vulnerable features. Laboratory tests resulted in 92% protection from convective heat and up to 96% protection from radiative heat.	[26]
Fire retardants	Laboratory investigation of fire-retardant treatment effect on firebrand production by wooden roofs. Wind tunnel experiments at 6 and 8 m/s found that roof assemblies (cedar shingles and cedar shakes) treated with retardant produced little or zero firebrands, while untreated assemblies produced more firebrands.	[27]
Acoustical extinction method	Laboratory experiments found the minimum sound pressure threshold to extinguish a burning and moving firebrand particle. 20 mm diameter dry wood spheres, ignited with a 250 W flame, are connected to a pendulum system to simulate firebrands. The extinguishment sound pressure threshold increases with sound frequency, and decreases significantly with increasing firebrand travelling speed.	[28]

on both firebrand and sand protection strategies; the review is focused on the driving processes of the protection strategies designs. The identified potentially applicable protection strategies design strategies inform the selection of two protection strategies—a trench and wall obstacle between the infrastructure and firebrand generation location—which are tested in exploratory FDS investigations. In this research, the firebrand contact exposure (the number of firebrands and the contact time duration between firebrands and the target obstacle) is assumed to correlate to the firebrand ignition probability of the target fuel, and is thus used as a measure of firebrand exposure hazard. Firebrand ignition dynamics are investigated in detail by numerous dedicated laboratory studies; the assumption correlating firebrand amount and contact time to firebrand ignition potential probability is based on a number of supporting conclusions from these experimental studies that are discussed in Section 4 [19–22]. The firebrand deposition and accumulation and firebrand ignition sub-processes are inherently connected and insights into the former has crucial implications and for the latter.

1.2 | Firebrand Protection Strategies

Current firebrand protection strategies and recommendations for UI buildings consist of maintaining defensible space in the immediate surroundings of the building to prevent indirect firebrand ignition, selecting fire-resistant building materials and installing vent screens protection on openings to prevent firebrand entry within the building (direct firebrand ignition). More specifically, WUI-tailored building construction regulations, the Australian Standard of buildings in bushfire-prone areas, the California Building Standard Chapter 7A, and the International Code Council WUI Code [23], require screen with openings area ranging from 0.03 to 0.40 cm^2 [24]. A recent systematic review of international WUI fire safety codes and standards highlighted a lack of codes focusing on building construction and especially on firebrand exposure threat [23]. Recent literature includes few studies of novel firebrand protection strategies. Table 2 lists the publications, along with a brief description, related to buildings firebrand ignition protection.

1.3 | Sand Protection Strategies

To meaningfully connect and learn lessons from the mature research field on sand hazard and accumulation [29] on infrastructure, this work reviews sand mitigation strategies to explore their applicability for firebrand direct ignition mitigation. In desert and coastal environments, sand has been observed to pose a hazard on infrastructure causing sedimentation on and erosion of the built environment [30]. Sand can compromise infrastructures in different manners; including accumulated sand posing lateral pressure on walls or increasing vertical load on roofs causing damage, sand entering and accumulating inside structures preventing normal performance, and sand covering railway tracks inhibiting proper function for rail operation. Threshold levels for limiting sand hazard performance have been defined through modelling research [31], and a variety of protection strategies have been applied and investigated to limit this impact.

Although there are inherent differences between sand and firebrand hazards on infrastructure, there are also important similarities. Figure 1 summarises the major qualitative differences and similarities between sand exposure and firebrand exposure hazards. The nature of the sand and firebrand particles is similarly characterised by widely distributed particles' chemical composition, mass, size, and shape. Both materials consist of

10991018, 2025, 5, Downloaded from https://onlinelibrary.wiley.com/doi/10.1002/fam.3286 by Imperial College London, Wiley Online Library on [07/07/2026]. See the Terms and Conditions (https://onlinelibrary.wiley.com/terms-and-conditions) on Wiley Online Library for rules of use; OA articles are governed by the applicable Creative Commons License

solid, irregularly shaped particles which vary in their physical and chemical characteristics depending on geographical location and generating processes.

Particle size and morphology of soil grains has been extensively studied due to its importance in influencing associated physical, mechanical and hydraulic soil properties [32]. According to the ISO 14688-1:2017, which standardises granular soil characterisation for engineering purposes, sand is considered coarse soil with particle diameters ranging between 63 μm and 2 mm [33]. Firebrand particles are larger. Firebrand size distributions reported in literature repot the majority of firebrands generated from vegetation have maximum diameters between 5 and 25 mm, while firebrands generated from structural fuels have maximum diameters between 16 and 56 mm [34]. Minimum firebrand diameter ranges are reported less often, literature indicated firebrands with diameters < 1 mm do occur; firebrands generated from a full structure burn were reported to have minimum 5 mm diameters [35]. Diameter ranges are indicative given the varying degrees of shape irregularity of soil particles and here calculated assuming circularity of the reported particle projected area. There are a number of quantitative shape descriptors that account for particle shape irregularity based on 2D shape characteristics (e.g, circularity [36, 37]) or 3D characteristics (e.g., sphericity [38], flatness and elongation [39]). Quantitative considerations for firebrand particle shape irregularity have only been considered through drag models which consider the particle sphericity [40] and a recently presented framework for firebrand 3D morphology characterisation [34]. Furthermore Tohidi et al. [41] concluded through geometric scaling analysis and validation with literature data that, for firebrand particles, the surface area scales with the mass raised to the power of 2/3 [41].

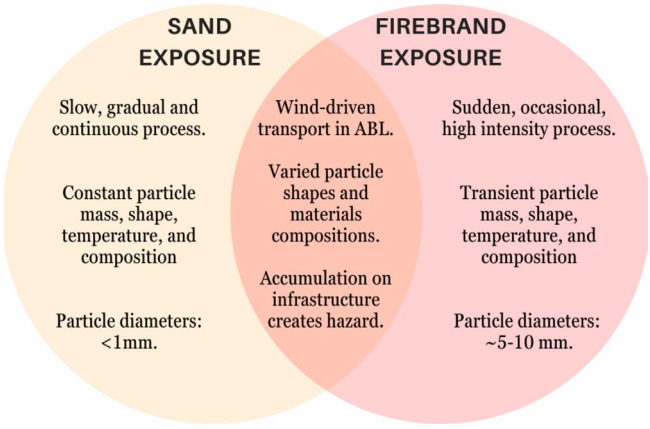


FIGURE 1 | Venn diagram comparing sand hazard characteristics, to wildfire firebrand hazard to infrastructure.

Firebrand particles are involved in ongoing thermal degradation and combustion reactions, and the heat they transfer to the target solid obstacles they interact with defines the hazard impact. Although both exposure processes include particulate transport in the atmospheric boundary layer processes, sand transport and accumulation is a relatively slow gradual and continuous processes over long temporal scales, while firebrand exposure is sudden, occurs occasionally during wildfire events, and is characterised by high intensity temperatures and wind. Sand particle exposure always originates from the ground level, while firebrand exposure includes the complexity of varying generation location and heights.

Numerous different sand mitigation strategies have been explored in literature and applied as practical infrastructure protection. This section reviews these strategies through a recently proposed characterisation measure, which divides mitigation strategies based on which part of the component in the sand-infrastructure interaction system is influenced; 'the source, path, and receiver' characterisation [42]. The mitigation strategies are classified based on whether they act on the particle origin location, transport trajectory location, or target location. These location areas are labelled in the Figure 2 schematic for both sand hazard and firebrand hazard.

Origin mitigation strategies aim to reduce the amount of wind-blown sand by either modifying the sand properties themselves, or the local wind flow field at the origin location of wind-blown sand. Examples include layer systems, protection methodologies that increase the sand bed moisture content thus increasing the cohesive forces between sand grains and the wind velocity threshold necessary to mobilise sand [43], and hedge systems, obstacles designed and placed on sand beds which increase the

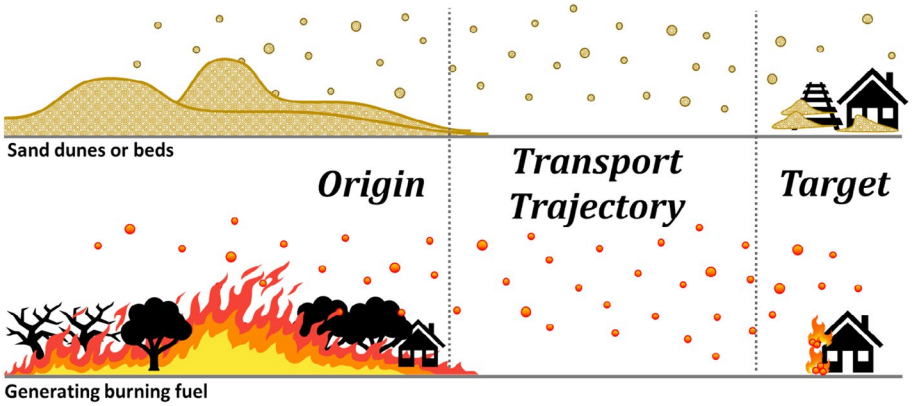


FIGURE 2 | Diagram illustrating the origin, transport trajectory, and target parts of the sand-infrastructure and firebrand-infrastructure interaction systems.

10991018, 2025, 5, Downloaded from https://onlinelibrary.wiley.com/doi/10.1002/fam.3286 by Imperial College London, Wiley Online Library on [07/07/2026]. See the Terms and Conditions (https://onlinelibrary.wiley.com/terms-and-conditions) on Wiley Online Library for rules of use; OA articles are governed by the applicable Creative Commons License

ground aerodynamic roughness, reducing the shear stress of the exposed sand bed [44, 45].

For firebrand exposure, the layer origin mitigation strategies can be potentially transferred over for application. Moisture or chemical modification to generating firebrand fuel can reduce the amount of firebrands generated from a given flaming fuel; an example is fire retardant impact on urban wooden fuel firebrand production was investigated [27]. Contrastingly, origin hedge mitigation systems for firebrands will likely not be especially effective because in contrast to sand which is lifted from the ground by the local wind flow, firebrand originate from a higher lofted height; therefore, modifying the particle aerodynamic properties at the generating origin location will likely not impede their transport. Furthermore, the generating origin will involve a wildfire, an uncontrolled burning location with smoke plume and highly transient aerodynamic conditions. Given these limitations for origin mitigation strategies this paper focuses the exploratory computational investigation on transport trajectory mitigation strategies.

Transport trajectory mitigation strategies impact the aerodynamic forces driving wind-blown particulate hazard, by focusing on modifying the flow field in the location of the particle trajectory between the origin location and the target infrastructure [42]. Solid obstacles in the trajectory location are introduced to promote particulate sedimentation by decreasing wind speed along the trajectory and inducing flow recirculation in designed areas. A number of mitigation strategies following this principle have been applied against sand [46] and snow [47] accumulation as (i) fences altering the wind flow towards the impacted infrastructure, and (ii) as ground surface geometry modifications, for example, creating trenches. All strategies promote the sedimentation of sand in a safe area away from the protected infrastructure. The orientation of the protecting fences or features is significant; the best practice approach in sand mitigation is to design the features with a 90° between the fence longitudinal axis and the prevailing wind direction expected to drive the particulate flux [42]. Both experimental and computational investigations of the aerodynamics and particulate sedimentation behaviour occurring around various types of fences are available in literature [48, 49]. The surface geometry modifications are influence by their size and geometry (determine by their height, width, and the slope of their contours). In this paper we present a simple preliminary analysis, using FDS, testing the applicability of a trajectory surface geometry trench mitigation measure for firebrand protection.

Lastly, the target mitigations are protections installed directed on the potentially impacted infrastructure. Aerodynamic-based target mitigation strategies protect specific portions of the infrastructure by impeding accumulation of sand particles on crucial infrastructure components, and modifying the particulate wind-driven trajectory by accelerating the particulate flow over the crucial infrastructure and encouraging deposition and accumulation in safe areas which do not disturb the infrastructure [42]. Patents for these protection systems applied to sand [50] and to snow [51] are available. Similar protection systems can be applied to firebrand ignition vulnerable building components; such as gutters, where dry vegetation can often accumulate and wildfire firebrands can easily land and ignite combustibles, or over decks and porches. Target mitigation strategies can also modify the target itself, through specific material selection and design to render the target exposure-resistant. Using fire-resistant materials, and applying finely-meshed screens to any vents or openings, are examples of available target-protections proposed and applied to protect building targets from firebrand exposure.

Modifying the aerodynamic conditions along the pathways of airborne particles as they are travelling towards infrastructure to limit their exposure can be an effective protection measure for wildfire firebrand exposure. This is the most easily mitigation measure computationally; to investigate the applicability of a trench protection measure, and a wall obstacle protection, simplified exploratory FDS simulations testing these two obstacles under varying wind conditions. The results are compared to a domain without these protection strategies to quantify the potential reduction in wildfire firebrand exposure and final contact with building structures.

2 | Methodology

This section outlines the computational approach used to estimate firebrand exposure under varying conditions. FDS is used to simulate firebrands as Lagrangian particles [52]. Lagrangian particles momentum contribution is represented through a force term $\left(\overrightarrow{f_b}\right)$ included in the gas phase conservation of momentum equation, which considers all momentum transferred from sub-grid Lagrangian particles to the fluid in a grid cell. The FDS Lagrangian model considers two-way coupling between the particle and fluid; therefore, momentum transfer is only considered between the particles and carrier fluid, particle-particle interaction and influence are neglected [53]. This sub-grid force term is calculated by Equation (1) and computes the forces transferred from the particles to the surrounding fluid flow in a given grid cell. The force term is related through Newton's second law of motion to the particle acceleration, neglecting rotational and translational forces acting on the particles; each particle acceleration, velocity and position are then resolved using Equation (2). C_d is the drag coefficient, A_p is the particle cross-sectional area, r_p is the particle radius, ρ is the gas density, $\vec{u}$ is the gas velocity, $\overrightarrow{u_p}$ is the particle velocity, and m_p is the particle mass [53].

$$\overrightarrow{f_b} = \frac{1}{V}\sum\left[\frac{1}{2}\rho C_d A_p\left(\overrightarrow{u_p}-\vec{u}\right)\left|\overrightarrow{u_p}-\vec{u}\right| - \frac{dm_p}{dt}\left(\overrightarrow{u_p}-\vec{u}\right)\right] \quad (1)$$

$$\overrightarrow{a_p} = \frac{d\overrightarrow{u_p}}{dt} = \vec{g} - \frac{1}{2m_p}\rho C_d A_p\left(\overrightarrow{u_p}-\vec{u}\right)\left|\overrightarrow{u_p}-\vec{u}\right| \quad (2)$$

Once the particles come to contact with a solid boundary, the default FDS 6.7.7 setting essentially simulates zero friction between particles and solid boundaries is applied. The force balance around particles continues to be solved, neglecting friction force effects and considering the local flow conditions; particles reach quasi-static accumulation when in a recirculation zone area where the drag force acting on the particle confines particle movement to a specific region (e.g., re-entrant solid boundary

10991018, 2025, 5, Downloaded from https://onlinelibrary.wiley.com/doi/10.1002/fam.3286 by Imperial College London, Wiley Online Library on [07/07/2026]. See the Terms and Conditions (https://onlinelibrary.wiley.com/terms-and-conditions) on Wiley Online Library for rules of use; OA articles are governed by the applicable Creative Commons License

corners), or the fluid force acting on the particle is below the minimum threshold to move particles (e.g., in static flow wake region). The FDS Lagrangian particle model has been verified for short-range firebrand transport for constant-mass particles with a spherical drag model simulating cubiform particles, and the cylindrical drag model simulating cylindrical particles [14]. FDS software (in some cases with FDS code modifications to account for rotational and translational forces acting on the particles, change in particle diameter due to charring, or sphericity corrections to account for particle irregular shapes) has since been applied in a number of studies to estimate firebrand exposure and transport dynamics [12, 15, 18, 54, 55].

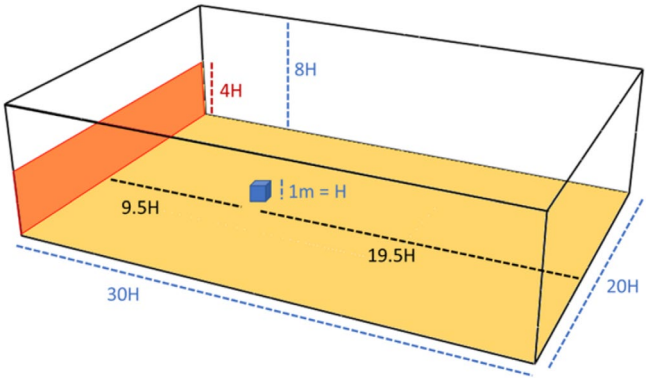


FIGURE 3 | Computational domain set up and dimension. Red rectangle corresponds to firebrand particles inlet vent location and blue cube is the obstacle structure representing a building.

2.1 | Computational Domain

The computational domain is illustrated in Figure 3; a 1 m high cube represents a simplified structure. The boundary conditions are summarised briefly in Table 3; further justification and validation of the wind and firebrand inlet boundary are provided in Sections 2.2 and 2.3. The cube geometry is chosen due to the availability of pressure coefficient (C_p) data measured in full scale (6 m cube) experiments which are used to validate the simulated wind flow impact [56] in Section 2.2. Furthermore, cube structures have been used both experimentally and computationally as simplified building structure obstacles to investigate firebrand exposure patterns around the building [15, 17]. The computational domain dimensions follow computational wind engineering best practice guidance to allow for realistic wind development and interaction around the investigated obstacle; best practices suggest to include space within the domain of 5 times the obstacle height upwind and around the lateral sides of the obstacle, and

TABLE 3 | Computational domain boundary conditions.

Boundaries	Boundary condition
Wind and firebrand inlet	Wind is introduced with a constant vertical profile, except for ground friction effects. Particles are introduced in the bottom half of the domain side, with the same velocity as the wind speed is set to
Top, remaining later boundaries	Open
Bottom	Inert

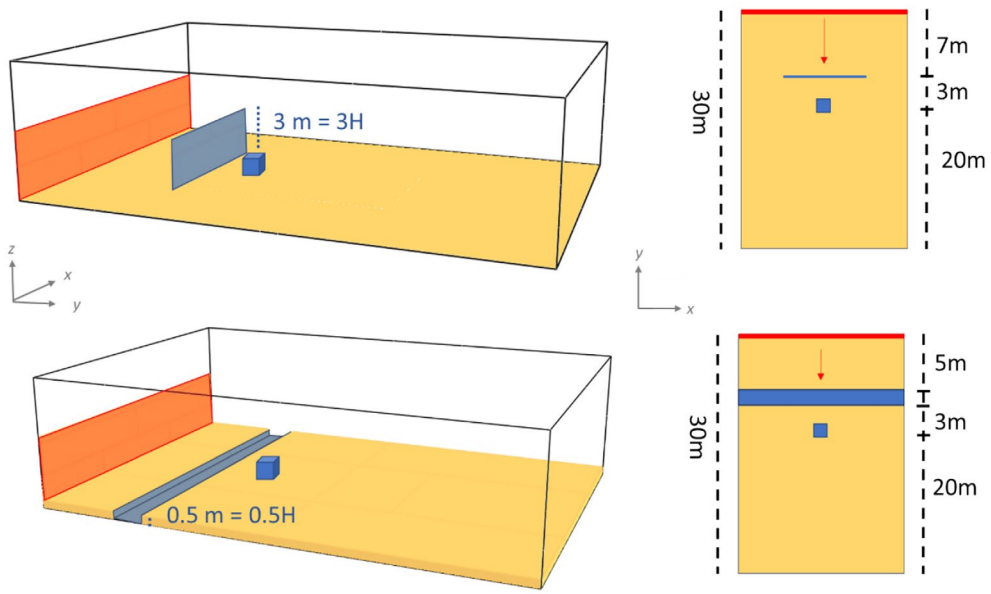


FIGURE 4 | Computational domains with wall (top) and trench (bottom) protection strategies. Red rectangle indicates firebrand particle inlet vent location, objects highlighted in blue indicate obstacles and protection strategies.

10991018, 2025, 5, Downloaded from https://onlinelibrary.wiley.com/doi/10.1002/fam.3286 by Imperial College London, Wiley Online Library on [07/07/2026]. See the Terms and Conditions (https://onlinelibrary.wiley.com/terms-and-conditions) on Wiley Online Library for rules of use; OA articles are governed by the applicable Creative Commons License

of 10–15 times the obstacle height length downwind of the obstacle to properly resolve vortex shedding in the wake region [57]. A trench protection with dimensions (2 m × 0.5 m) across the entire computational domain width and a wall protection of dimensions (10 m × 3 m) are tested, as shown in Figure 4.

A grid sensitivity analysis was conducted by running a simulation (4 m/s reference wind speed, without protection obstacles) with three different uniform cell sizes in the computational domain's finest mesh: 3.33, 5, and 10 cm. Figure 5 presents the final (at 400 s) particles positions distribution for each grid tested; the average particle position differs by 8.2% between the medium and finest grids tested, and by 18.8% between the medium and coarsest grids. 8.2% is considered an acceptable difference for the presented simulations and the 5 cm uniform grid size is selected. The 5 cm cell size is applied in the mesh containing the cube obstacle and immediate surroundings. The surrounding meshes in the $z < 2$ m portion of the domain have uniform cell sizes of 10 cm, the meshes located in the $2\text{ m} < z < 4$ m domain portion have 20 cm cell sizes, and the top domain portion ($z > 4$ m) have 40 cm cell sizes of.

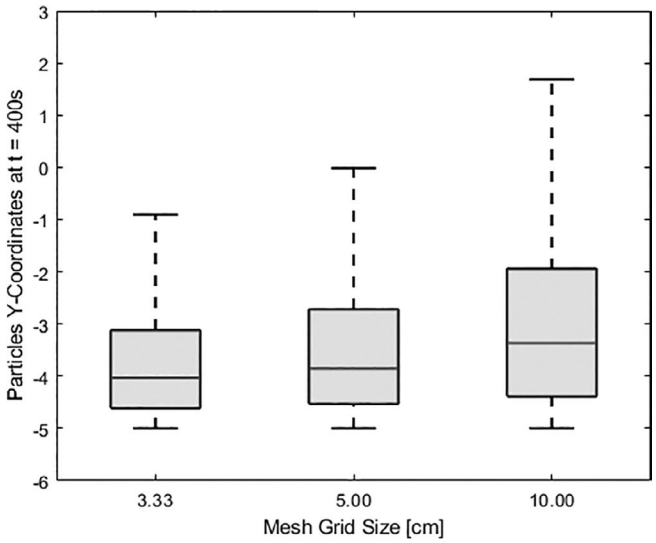


FIGURE 5 | Grid sensitivity analysis results for the particles position distributions for tested uniform grid sizes of 3.33, 5.00, and 10.00 cm for the 4 m/s reference wind speed scenario at 400 s.

2.2 | Wind Load

The wind is introduced with a simple constant wind profile in the z direction, except for friction impacts with the solid ground; given the simplified nature of the computational domain tested, and the exploratory purpose of the simulations the flow profile is chosen to be maintained as simple as possible to investigate the relative behaviour of the particles under increasing flow speeds. FDS considers turbulence by Large Eddy Simulation (LES); simulations are conducted with the default Deardorff turbulence viscosity model. The wind load on the cubic structure simulated is verified by comparing experimental results. Pressure coefficient measurements are compared to well-established, full scale field experimental measurements by Richards and Hoxey [56]. Results of the pressure coefficients comparison is shown in Figure 6 [56]; the average difference between the two measurements is 6.3%

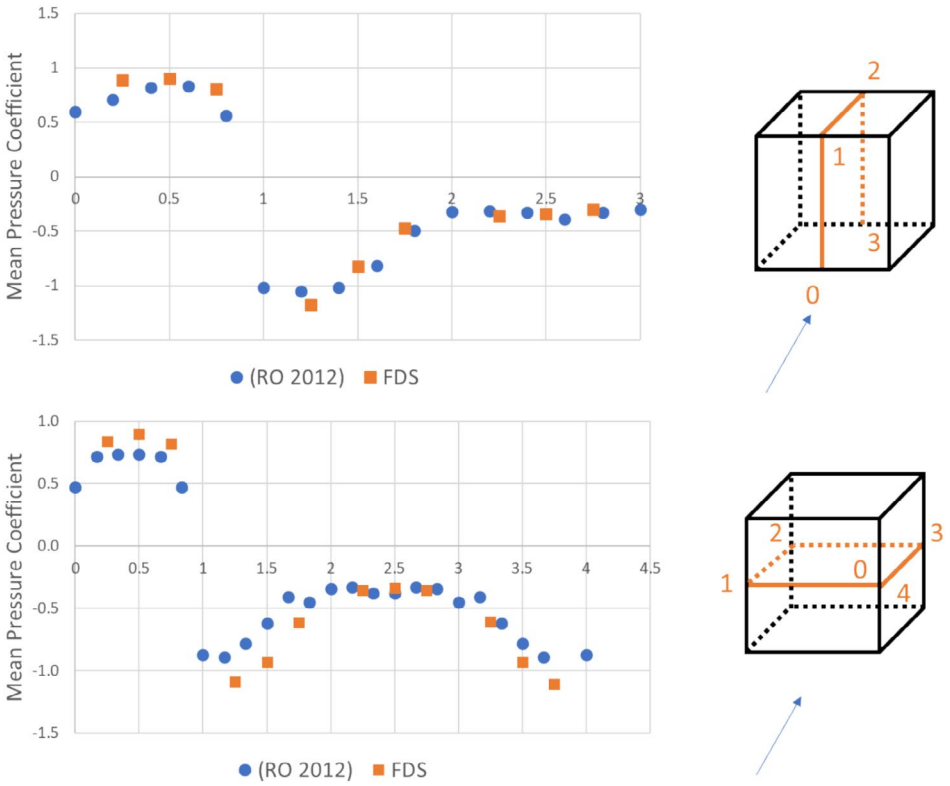


FIGURE 6 | Pressure coefficients measured on FDS cube obstacle comparison with field measurements of wind load on full scale 6 m cube structure by [56].

10991018, 2025, 5, Downloaded from https://onlinelibrary.wiley.com/doi/10.1002/fam.3286 by Imperial College London, Wiley Online Library on [07/07/2026]. See the Terms and Conditions (https://onlinelibrary.wiley.com/terms-and-conditions) on Wiley Online Library for rules of use; OA articles are governed by the applicable Creative Commons License

for the vertical ring measurements, and 5.2% for the horizontal ring measurements.

2.3 | Lagrangian Particles

Non-combusting, constant mass, Lagrangian particles are introduced in the domain to simulated wildfire firebrand particles. The particle inlet vent height is 4 times the cubic obstacle height in the domain, and particles are introduced throughout the vent height to simulate a simplified wildfire flaming front producing firebrands at various heights. Burning surface fuel during wildfires can generate firebrands at various heights and the simulations introduce firebrands continuously in the z-direction within the inlet vent to account for this. This approach overestimates the area size generating firebrands to produce conservative results in terms of number of firebrands generated. Table 4 summarises all particle and particle inlet properties, along with appropriate literature references explaining the values selected. To prescribe the specific firebrand inlet flux selected, particles are prescribed to be introduced in the domain every 20 s, the inlet is not continuous but periodic temporally; results are analysed considering the full temporal simulation duration and allow the wind profile full development before introducing particles to mitigate this limitation. The Tachikawa (K) dimensionless number [63], the ratio of aerodynamic forces to gravitational forces acting on airborne object, is given by Equation (3) where ρ_f is the air density, ρ_p is the firebrand particle density, u is the reference wind speed, g is the gravitational acceleration and $\overline{d}_p$ is the average particle density. K has been used to interpret firebrand wind driven transport and landing [27] and estimate critical threshold values above which firebrands are not expected to accumulate for a given target obstacle and wind direction [62].

$$K = \frac{\rho_a u^2}{\rho_p g \overline{d}_p} \tag{3}$$

3 | Results

3.1 | No Protection

Results analysis aims to quantify the particles position and proximity to the cubic structure and compare the particle position patterns amongst the different computational domain arrangements. To quantify the cumulative contact of all particles simulated with the ground floor over the entire simulation temporal duration, the particle positions are integrated over the simulated time they spend on the ground floor, and counted for 0.01 m^2 grid sections of the computational domain floor. The resulting histograms are normalised, resulting in heat maps illustrating the relative particle landing density across the domain floor, throughout the entire simulation time. The particle contact-exposure graphs quantify the simulated particle contact heat maps with values ranging from 0 to 1; where 0 indicates no firebrands reaching the solid ground area in question, and 1 corresponds to the maximum amount of firebrand particles coming to contact with the indicated 0.01 m^2 area for the maximum amount of simulated time. Figure 7 presents these results for the no protection case, for each reference wind speed tested; results are presented for the finest mesh grid in the computational domain.

To compare the particle position patterns at the final simulation time step and the corresponding flow patterns, contour and heatmaps graphs are computed. Figures 7–9 show the particle position, particle landing density, and average wind flow v-velocity component at $z = 0.15$ m at 300 s of the simulation for reference wind speeds 4, 6, and 8 m/s respectively. Time 300 s is selected to characterise particle location because both the flow field and the particle position have reached steady state by this time in the slowest reference wind speed scenario tested.

TABLE 4 | Lagrangian particle properties simulated in FDS and the related literature references.

	FDS Lagrangian particles	Firebrand particles literature
Shape	Spherical	FDS Validation for short-range transport [14].
Radius	Normally distributed between: 0.0030 and 0.0075 m	80% particles: $A_p = 0.1–20 \times 10^{-5}$ m^2 [58]. Density of landing density varies between 355 and 467 kg/m^3 [12]; initial firebrand landing distributed between 50 and 300 kg/m^3 [59]. Mass distribution of 250 urban fuel-generated firebrands collected, significant majority range between 0.001 and 0.5 g; only 2 firebrands were larger than 2.5 g [60].
Cross sectional area	2.8×10^{-5}–1.8×10^{-4} m^2	
Volume	1.1×10^{-7}–1.8×10^{-6} m^3	
Density	300 kg/m^3	
Mass	0.03–0.5 g	
Firebrand inlet flux to computational domain	3.8 particles m^{-2} s^{-1}	Flux to single story house, for max. wildfire radiative heat flux 20–120 kW/m^2 [12]: Low FDI: 2.6–5.6 particles m^{-2} s^{-1} High FDI: 1.7–3.6 particles m^{-2} s^{-1}
Tachikawa number	4 m/s wind: 0.67 6 m/s wind: 1.52 8 m/s wind: 2.70	2.6 [61] 2.19, 3.15, 3.41, 3.43, 5.06, 5.07, 5.17, 5.98, 6.44 [62]

10991018, 2025, 5, Downloaded from https://onlinelibrary.wiley.com/doi/10.1002/fam.3286 by Imperial College London, Wiley Online Library on [07/07/2026]. See the Terms and Conditions (https://onlinelibrary.wiley.com/terms-and-conditions) on Wiley Online Library for rules of use; OA articles are governed by the applicable Creative Commons License

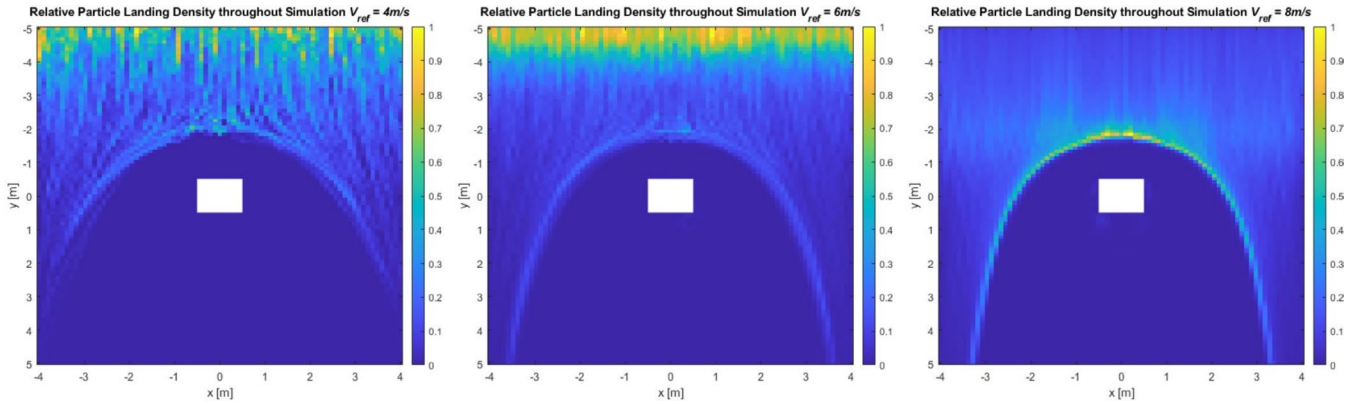


FIGURE 7 | Relative particle landing densities and contact time with computational domain ground floor around cubic obstacle (position indicated by white square) for each reference wind speed simulated (from left to right: 4, 6, and 8 m/s).

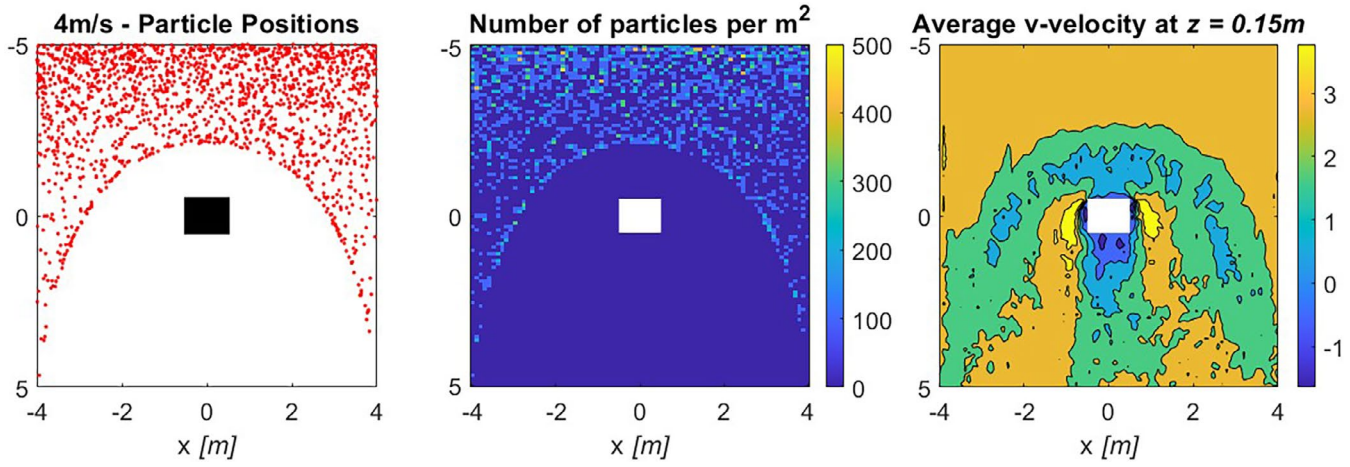


FIGURE 8 | Particle position and average v-velocity on the $z = 0.15$ m plane at time step = 300 s of simulation with reference wind speed 4 m/s. Cubic obstacle location shown by white square.

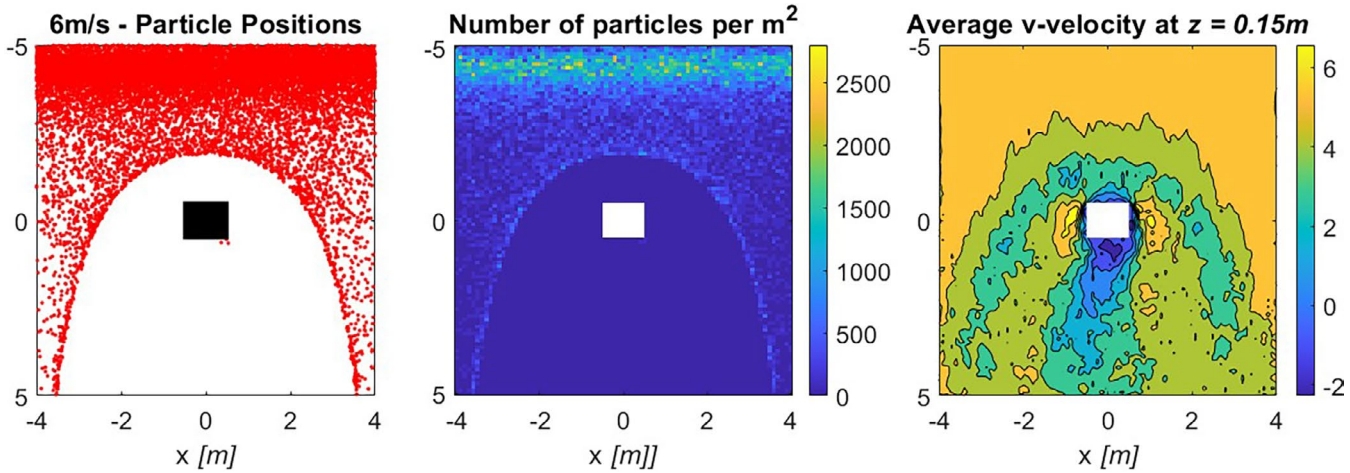


FIGURE 9 | Particle position and average v-velocity on the $z = 0.15$ m plane at time step = 300 s of simulation with reference wind speed 6 m/s. Cubic obstacle location shown by white square.

3.2 | Trench Protection

For the protection strategies tested, the relative firebrand particles landing density and contact time duration with ground floor are computed for a larger computational domain section; these are presented in Figures 11 and 15 for the trench and wall protection respectively. Results regarding the impact of the trench protection in the domain are presented first, showing the impact of increasing wind speeds of the particle position over the entire simulation (Figure 10), at the final time step simulations (Figures 11 and 12). The simulations involving the protection strategies are simulated until

10991018, 2025, 5, Downloaded from https://onlinelibrary.wiley.com/doi/10.1002/fam.3286 by Imperial College London, Wiley Online Library on [07/07/2026]. See the Terms and Conditions (https://onlinelibrary.wiley.com/terms-and-conditions) on Wiley Online Library for rules of use; OA articles are governed by the applicable Creative Commons License

200 s to limit computational resources; at this timestep the flow patterns are fully developed, and have reached a steady state configuration. To characterise the influence of the introduced protection strategies on the wind flow field of interest, the average velocity component in the y-direction (v-velocity) is averaged for the last 50 s of the simulation to estimate the streamlines and associated flow speeds created by the protection strategies introduced; there are provided in Figures 13

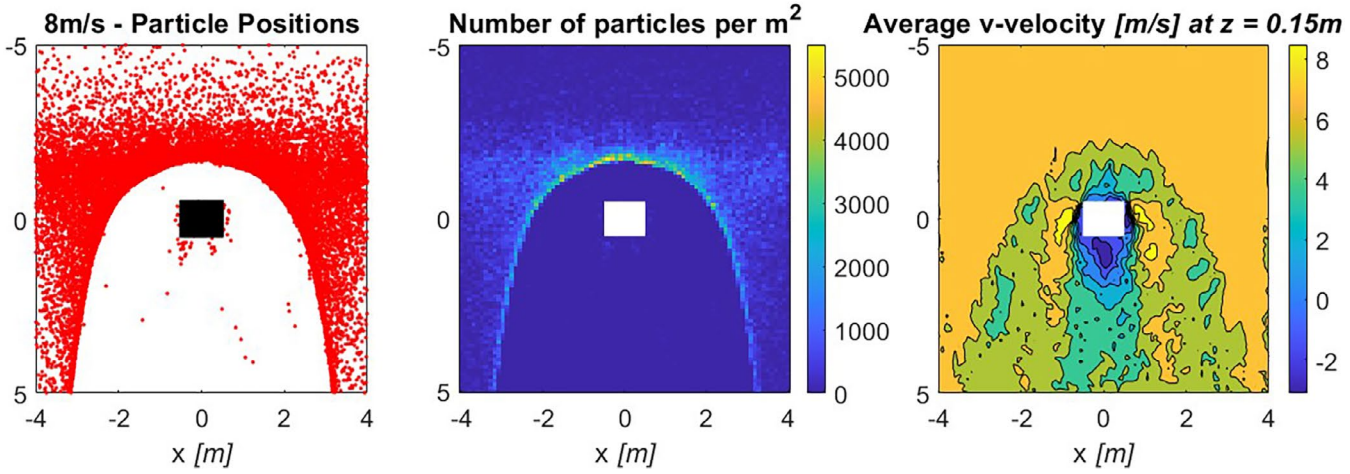


FIGURE 10 | Particle position and average v-velocity on the $z = 0.15$ m plane at time step = 300 s of simulation with reference wind speed 8 m/s. Cubic obstacle location shown by white square.

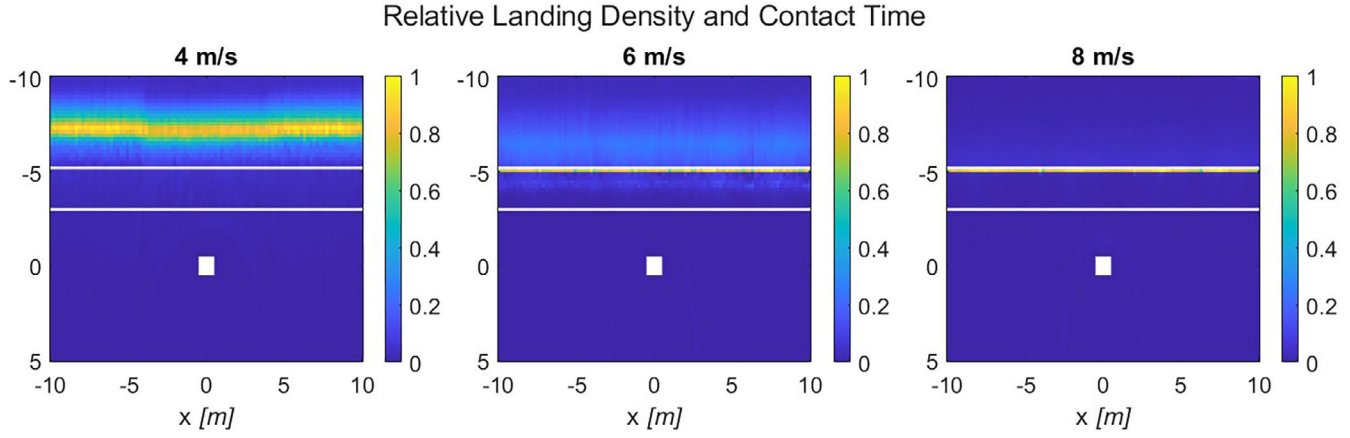


FIGURE 11 | Relative particle landing densities and contact time with computational domain ground floor around cubic obstacle (position indicated by white square) with trench protection measure (edges shown by white lines) for all wind speed simulated (from left to right: 4, 6, and 8 m/s).

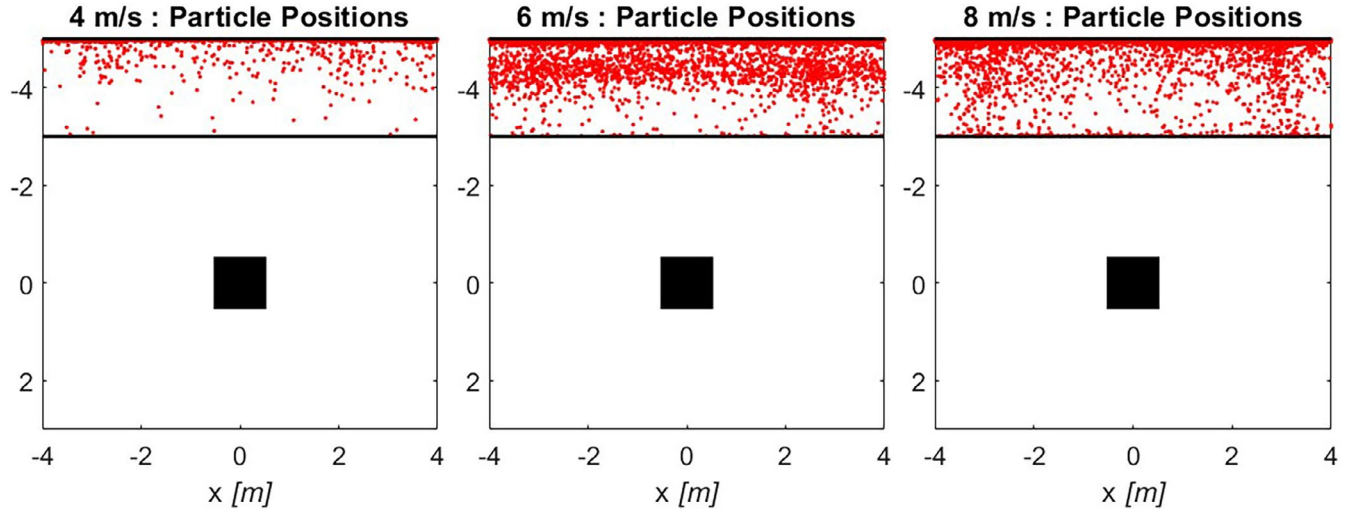


FIGURE 12 | The particle position at 200 s for the trench protection measure scenario for all reference wind speeds tested (from left to right: 4, 6, and 8 m/s).

10991018, 2025, 5, Downloaded from https://onlinelibrary.wiley.com/doi/10.1002/fam.3286 by Imperial College London, Wiley Online Library on [07/07/2026]. See the Terms and Conditions (https://onlinelibrary.wiley.com/terms-and-conditions) on Wiley Online Library for rules of use; OA articles are governed by the applicable Creative Commons License

and 17 for the trench protection and wall protection respectively (Figure 14).

3.3 | Wall Protection

See Figures 15–18.

3.4 | Quantifying Protection Effect

The particles' mass density in specific regions around the cubic obstacle structure and around the protection strategies are measured throughout the simulation; these measurements characterise particle accumulation in different regions of interest in the computational domain. The firebrand particles' mass is measured in a cuboid of 5 m × 5 m × 1 m dimensions surrounding the target cubic obstacle, and in two cuboids located within the trench protection and windward of the wall protection; particles' mass is also measured in the cuboid immediately above the cubic structure, this location did not record any significant particle accumulation and is therefore not included in the results. All measurement locations are shown in Figure 19. The particles' mass density is recorded in mass per unit volume (kg/m^3) in FDS, the measured particle density at the indicated locations is then normalised to the inlet particles mass per unit volume

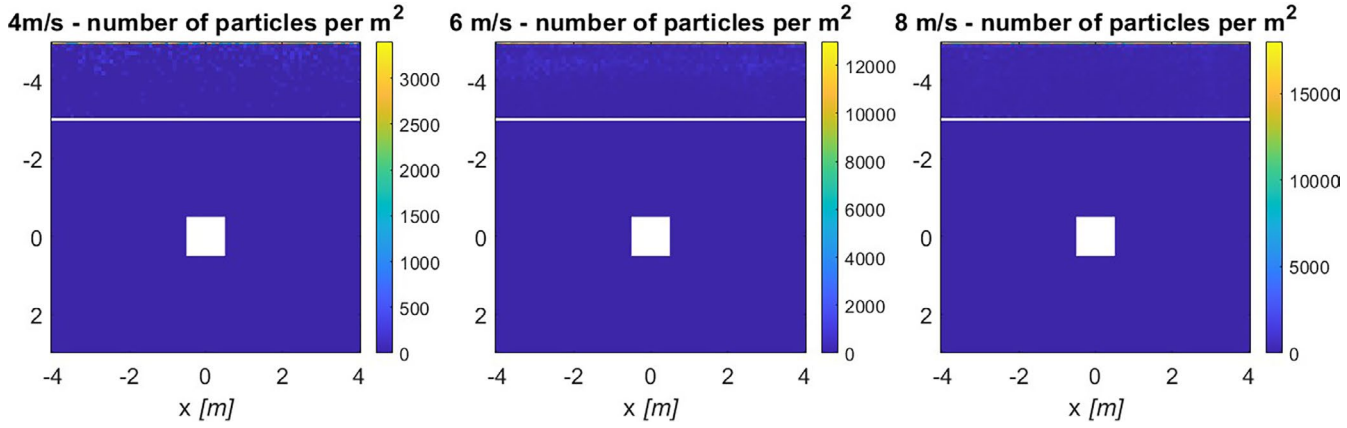


FIGURE 13 | The particle position and their landing density per ground floor m^2 at 200 s for the trench protection measure scenario with reference wind speed 8 m/s.

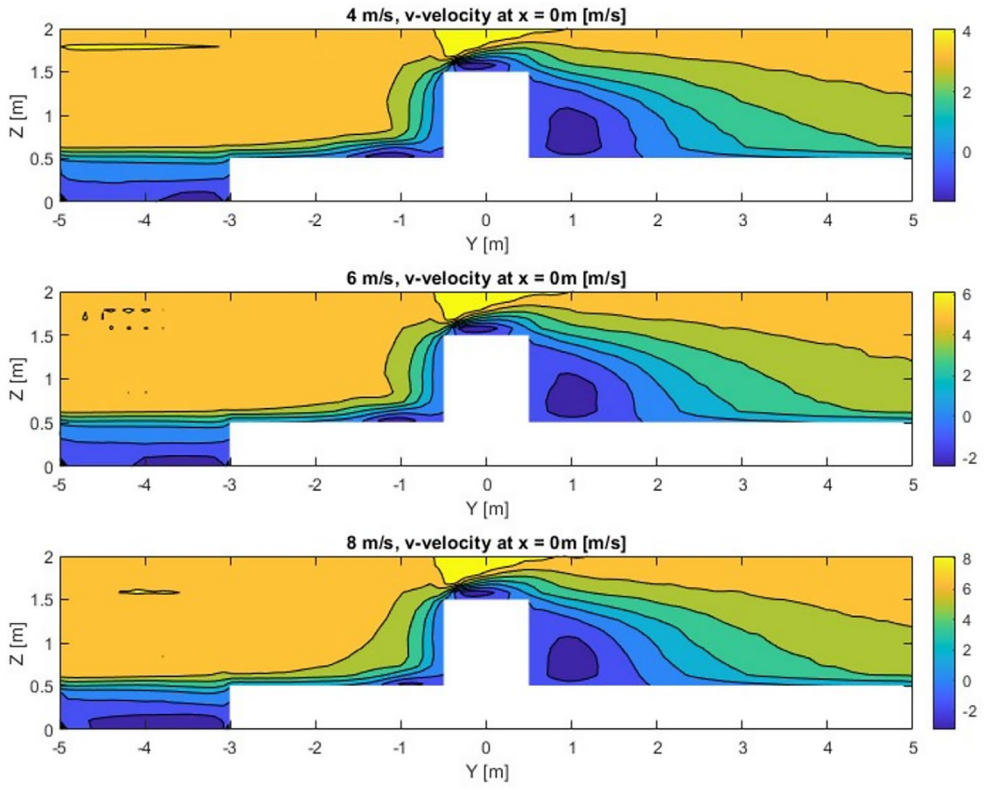


FIGURE 14 | Average v-velocity at $x = 0$ m, between 150 and 200 s, of central domain section for trench protection scenarios for all wind speeds simulation (from top to bottom 4, 6, and 8 m/s).

10991018, 2025, 5, Downloaded from https://onlinelibrary.wiley.com/doi/10.1002/fam.3286 by Imperial College London, Wiley Online Library on [07/07/2026]. See the Terms and Conditions (https://onlinelibrary.wiley.com/terms-and-conditions) on Wiley Online Library for rules of use; OA articles are governed by the applicable Creative Commons License

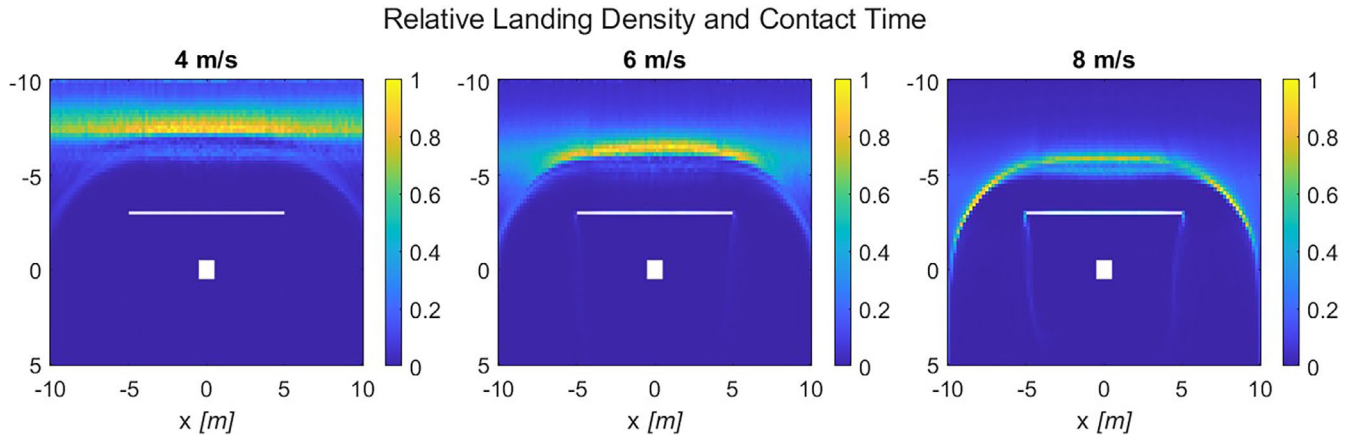


FIGURE 15 | Relative particle landing densities and contact time with computational domain ground floor around cubic obstacle (position indicated by white square) with wall protection measure (shown by white line) for all wind speed simulated (from left to right: 4, 6, and 8 m/s).

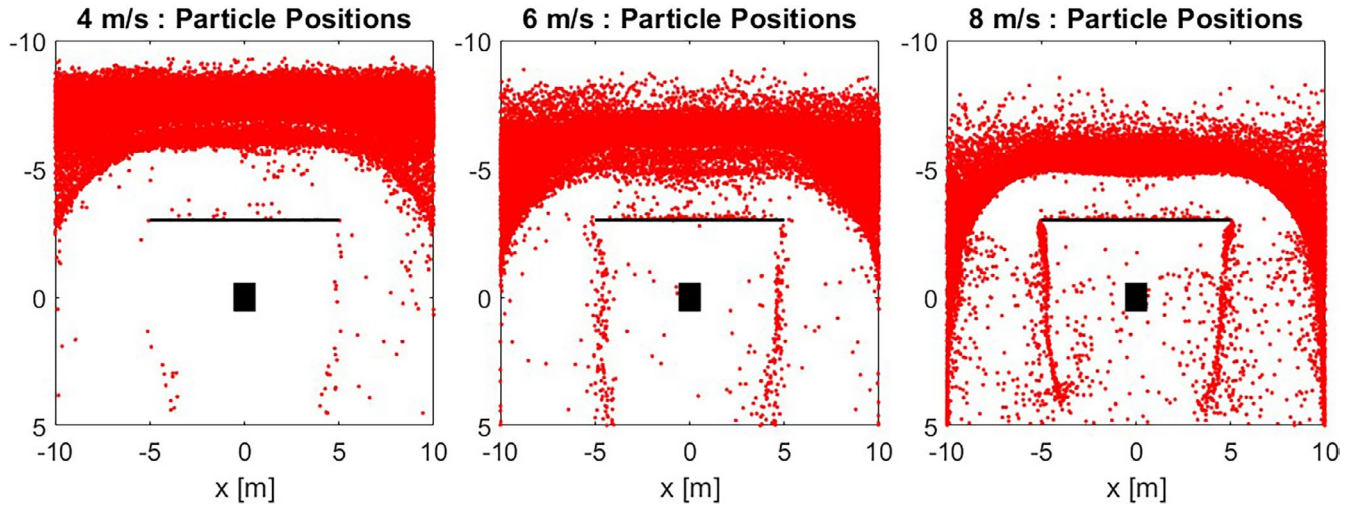


FIGURE 16 | The particle position at 200 s for the wall protection measure scenario for all reference wind speeds tested (from left to right: 4, 6, and 8 m/s).

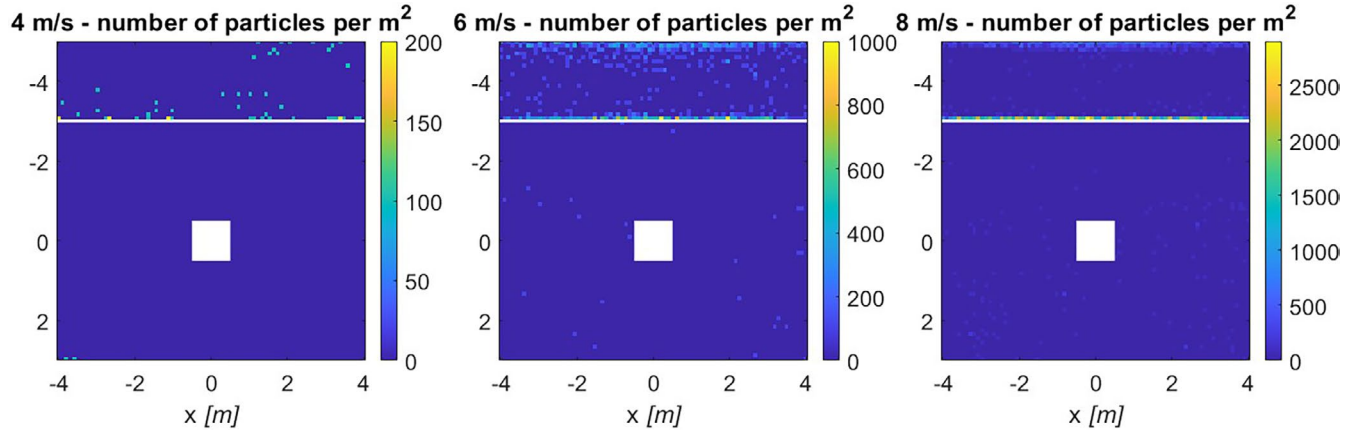


FIGURE 17 | The particle landing density per ground floor m^2 at 200 s for the wall protection measure scenario all reference wind speeds tested (from left to right: 4, 6, and 8 m/s).

10991018, 2025, 5, Downloaded from https://onlinelibrary.wiley.com/doi/10.1002/fam.3286 by Imperial College London, Wiley Online Library on [07/07/2026]. See the Terms and Conditions (https://onlinelibrary.wiley.com/terms-and-conditions) on Wiley Online Library for rules of use; OA articles are governed by the applicable Creative Commons License

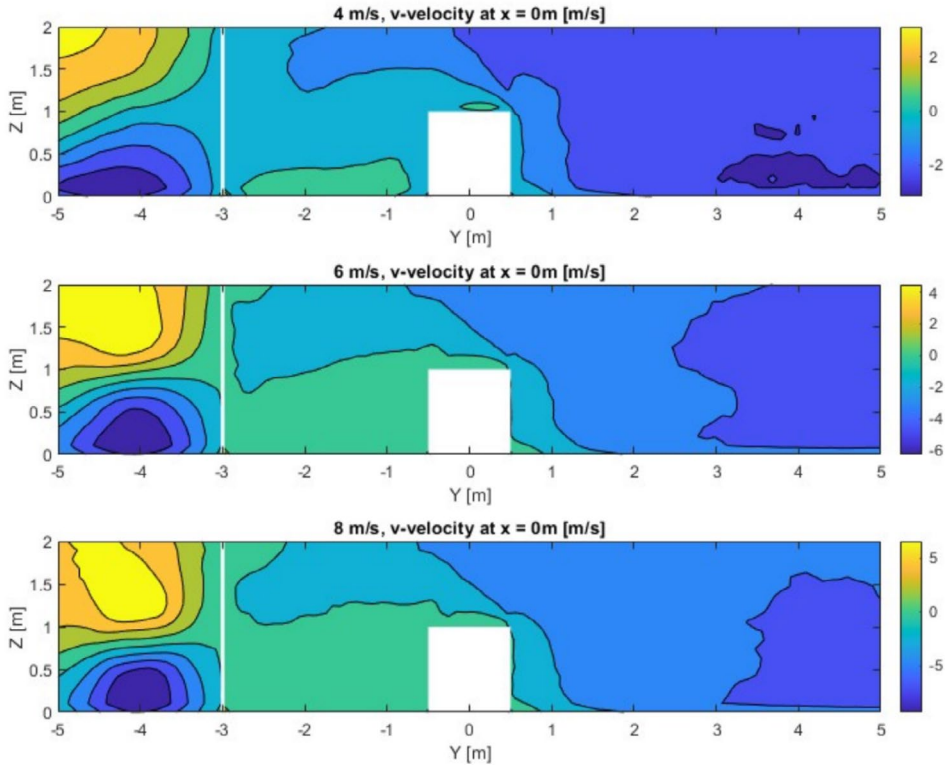


FIGURE 18 | Average v-velocity at $x = 0$ m, between 150 and 200s, of central domain section for wall protection scenarios for all wind speeds simulation (from top to bottom 4, 6, and 8 m/s).

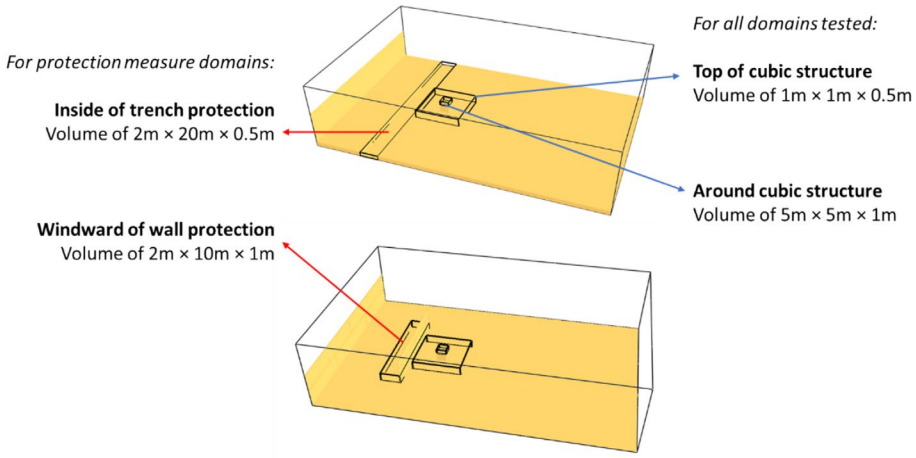


FIGURE 19 | Cuboid locations where firebrand particle mass is measured throughout simulations: Around the cubic structure in a volume of 25 m^3, on top of the cubic structure in a volume of 0.5 m^3, and within the trench protection and windward of the wall protection.

density, as indicated by Equation (3). Where $\emptyset_{fi}$ is the proportion of total inlet particles mass density in location i, $MPUV_i$ and $MPUV_{inlet}$ are the particles' mass per unit volume at location i and at the particle inlet respectively.

$$\emptyset_{fi} = MPUV_i / MPUV_{inlet} \quad (4)$$

Figures 20–22 compare the firebrands mass recorded in the volume surrounding the cubic structure for all protection strategies and all reference wind speeds tested; the measurements indicate the amount of particles that would reach the structure with and without the protection strategies considered. Results are presented as the proportion of inlet firebrand density, and suggest all protection strategies result in a significant decrease of firebrand flux reaching the cubic structure; the most effective reductions are measured for both protection strategies tested at 4 m/s reference wind speed, and for the wall protection measure tested at 6 and 8 m/s reference wind speeds. The two higher wind flow profiles tested (reference wind speed: 6 and 8 m/s), transport firebrands past the trench protection measure; thus, decreasing its removal effectiveness. The protection strategies dimensions and their related effectiveness should be tested for all expected wind profile in detailed design assessments. For the 4 m/s reference wind speed, the firebrand particles creep along

10991018, 2025, 5, Downloaded from https://onlinelibrary.wiley.com/doi/10.1002/fam.3286 by Imperial College London, Wiley Online Library on [07/07/2026]. See the Terms and Conditions (https://onlinelibrary.wiley.com/terms-and-conditions) on Wiley Online Library for rules of use; OA articles are governed by the applicable Creative Commons License

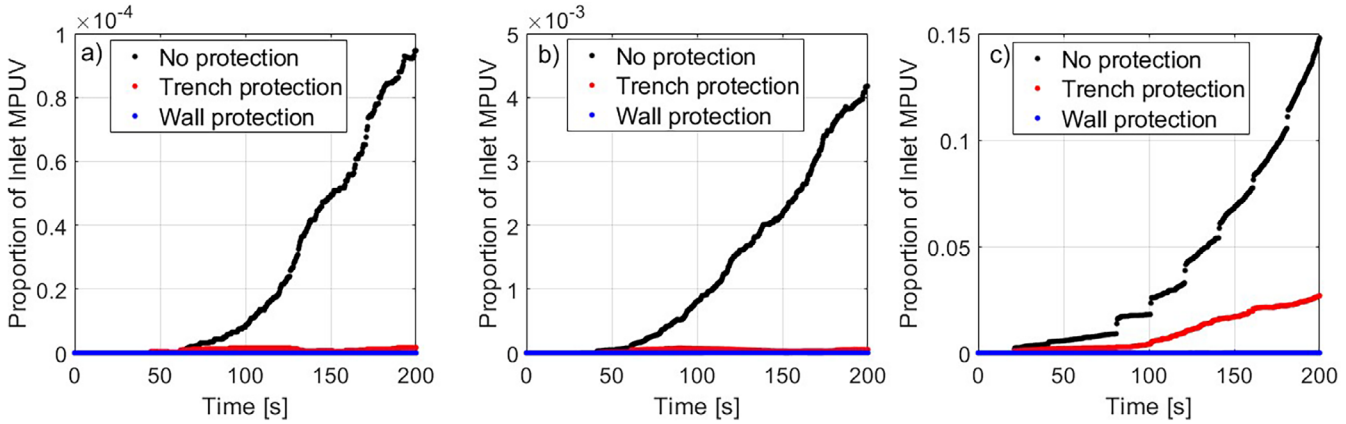


FIGURE 20 | Proportion of inlet firebrand particles mass density in cuboid volume surrounding the target cubic structure for no protection strategies (black), trench protection measure (red) and wall protection measure (blue) tested with (a) 4 m/s, (b) 6 m/s, and (c) 8 m/s reference wind speed.

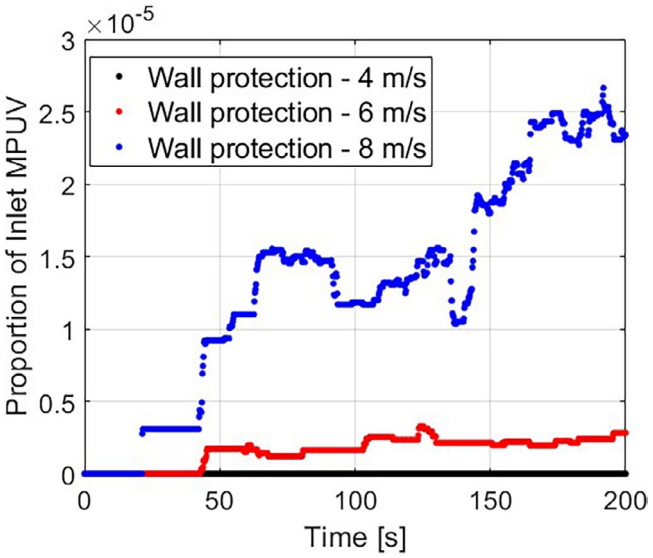


FIGURE 21 | Proportion of inlet firebrand particles mass density in cuboid volume surrounding cubic target structure with wall protection measure for all reference wind speeds tested.

the ground floor windward of the cubic structure before reaching structure; both protection strategies tested in this simplified domain for the 4 m/s reference wind speed are, therefore, extremely effective in preventing the particles from reaching the cube surroundings.

Table 5 summarises the maximum mass landing densities that are found in the 25 m^3 volume which immediately surrounds the cubic structure. For the highest reference wind speed tested, 8 m/s, there is a significant higher mass of particles recorded; reaching up to 5 orders of magnitude greater than the measured amount at the lowest wind speed tested, 4 m/s. This large difference is due to the accumulation of particles in the recirculation zones which occur around the cubic structure. The higher flow speeds transport a greater number of particles in the recirculation zones where they get entrained in the local flow patterns and accumulate; for the no protection strategies domain, the particles area surrounding the cubic structure reach 15% of the inlet density in 200 s. The flow speed in the recirculation zones also increases with the increasing reference wind speeds. In the simulations, accumulation is not caused or influenced by friction force, which is not considered in the FDS model, but rather due to the flow recirculation zones created which inhibit the particle movement. In reality, friction effects are expected to increase the particle accumulation, most probably in firebrand particle paths regions highlighted in Figures 6, 10, and 14. The best firebrand reduction performance is recorded for the wall protection measure. The wall obstacle's firebrand flux reduction to the cubic structure's immediate surroundings reaches 99% compared to the computational domain without protection strategies. It is important to note that the measurement region used to calculate the reduction does not include the windward area of the wall obstacle where many particles are redirected (shown clearly in Figures 14 and 15). This redirection is a critical phenomenon caused by modifications to the local flow field, which alter firebrand particle trajectories and shift their accumulation to a different location. Further analysis and care of such protection strategies' designs needs to ensure the redirected firebrands are transported to an area resistant to the expected associated heat exposure. As illustrated in Figure 17, the modified flow field around the cubic structure effectively prevents a significant number of particles from reaching and accumulating in its immediate vicinity.

The trench protection, in this idealised scenario results in a significant reduction of particle exposure around the cubic structure. At the final step of the simulation, the trench protection provides the highest percentage reduction (98%) in particles mass around the cubic structure, compared to the computational domain without protection strategies, for the 6 m/s reference wind speed. The variety in reduction performance observed for the different wind speeds indicates the sensitivity a trench type of protection has to the particle properties and local field conditions; specific conditions should be tested to confirm performance under various ambient conditions and obstacle layouts.

Figure 22 presents the firebrands mass proportion throughout the simulation duration that accumulates within the trench volume, and in the volume just windward of the wall protection measure; as illustrated in Figure 19. The trench protection volume receives firebrand mass steadily; as ambient wind speed increases so does the firebrand accumulation rate within the

10991018, 2025, 5, Downloaded from https://onlinelibrary.wiley.com/doi/10.1002/fam.3286 by Imperial College London, Wiley Online Library on [07/07/2026]. See the Terms and Conditions (https://onlinelibrary.wiley.com/terms-and-conditions) on Wiley Online Library for rules of use; OA articles are governed by the applicable Creative Commons License

trench, reaching 2.9 times the inlet firebrand density for the highest reference wind speed tested, 8 m/s. The firebrands mass measured windward of the wall obstacle indicate a steady accumulation rate pattern for the reference 8 m/s wind speed and a more transient accumulation rate for the 6 m/s wind speed. The firebrands are eventually moved leeward of the wall obstacle, following the recirculation zones which form around the wall, thus diverting the firebrands paths from reaching the leeward side of the cubic obstacle directly (Figure 23).

4 | Discussion

This work presents exploratory simulations using the FDS Lagrangian particle model, simulating non-burning spherical particles, to estimate the wildfire firebrand flux exposure towards a generic cubic obstacle, representing a simplified building structure, and how the firebrand flux exposure is affected by implementing protection strategies inspired by sand infrastructure protections. Current research on wildfire firebrand

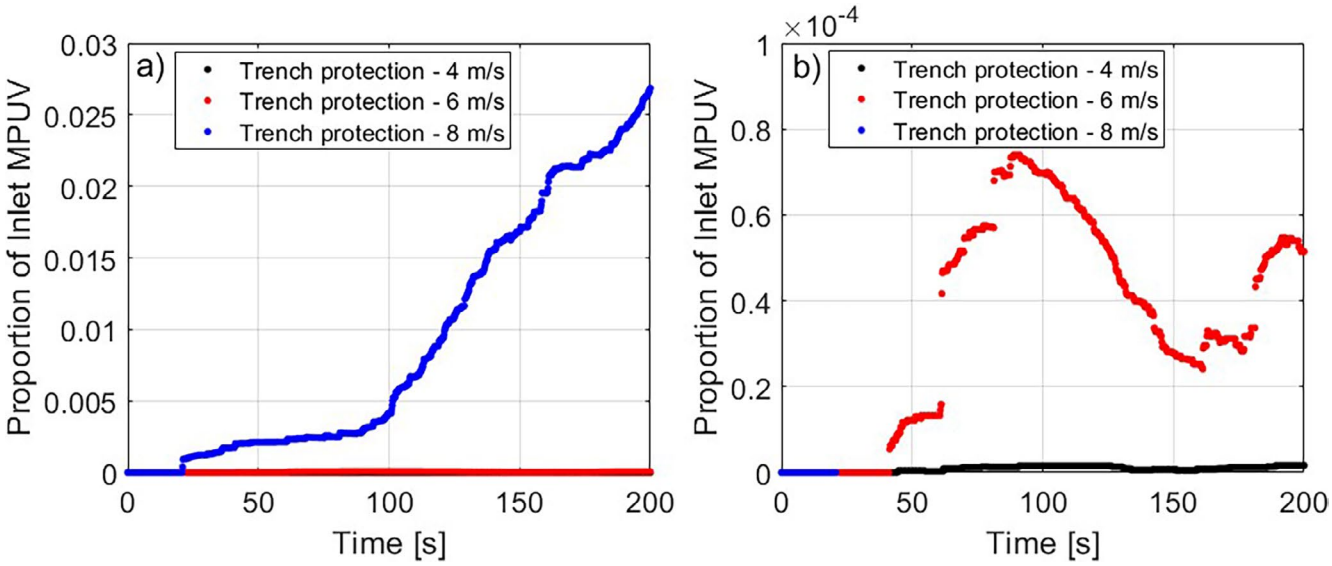


FIGURE 22 | Proportion of inlet firebrand particles mass density in cuboid volume surrounding target structure with trench protection measure for (a) all reference wind speeds tested (b) and zoomed to maximum 1×10^{-4} proportion, to visualise 6 and 4 m/s reference wind speeds results.

TABLE 5 | Maximum firebrand density in volume immediately surrounding the cubic structure for all computational domains tested.

	Only cube (g/m³)	Trench protection (g/m³)	Reduction (%)	Wall protection (g/m³)	Reduction (%)
4 m/s	0.0130	0.00230	82	0	100
6 m/s	0.132	0.00230	98	0.00386	97
8 m/s	203	36.8	82	0.0320	99

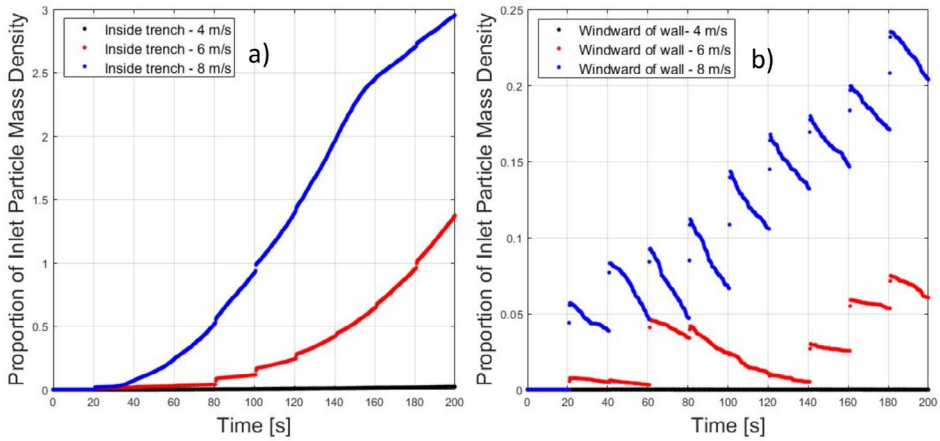


FIGURE 23 | Mass per unit volume of firebrand particles measured (a) inside the trench protection measure and (b) windward of the wall protection measure.

10991018, 2025, 5, Downloaded from https://onlinelibrary.wiley.com/doi/10.1002/fam.3286 by Imperial College London, Wiley Online Library on [07/07/2026]. See the Terms and Conditions (https://onlinelibrary.wiley.com/terms-and-conditions) on Wiley Online Library for rules of use; OA articles are governed by the applicable Creative Commons License

protection strategies is summarised, and parallels between sand accumulation and firebrand accumulation hazards are presented; the purpose of this research is to explore whether the same driving principles applied in implementing sand protection strategies can be extended to wildfire firebrand exposure hazard and protection. FDS simulations creating a simplified and conservative firebrand exposure scenario under three different ambient reference wind speeds (4, 6, and 8 m/s) are presented without any protection, with a wall protection, and a trench protection to investigate their feasibility.

This research assumes that firebrand contact exposure, defined as the number of firebrands and their contact duration with the target obstacle (plotted in Figures 7, 11, and 15) correlates to the firebrand-induced ignition probability of the target fuel. This assumption relates firebrand contact exposure to expected firebrand ignition hazard. A number of dedicated experimental and theoretical investigations have been conducted in literature to investigate firebrand ignition dynamics; conclusions from various studies indicate a correlation between ignition potential and amount of firebrand flux, or closer spacing between firebrands (up to a critical separation distance between firebrands) [19–22, 64].

Kwon and Liao [64] experimentally measured the influence of spacing distance between burning firebrands on their combustion dynamics, and observed that decreasing spacing between firebrands increased flame height and mass loss rate, up to a threshold spacing distance which, when surpassed, limits combustion due to air entrainment; smouldering firebrand piles burned hotter and longer compared to single firebrands [64]. Zhu and Urban [22] conducted an experimental and numerical study to investigate conditions associated with firebrand accumulation and associated ignition potential; findings show that when a second firebrand is introduced within a critical distance to the first, the target fuel ignition is faster or requires lower incident heat flux [22]. Suzuki and Manzello [21] experimentally investigated the combined effect of firebrand exposure and external radiant heat and found that higher wind speeds and longer preheating time, correlate with lower time to ignition; furthermore, increasing wind speeds resulted in firebrands contributing increasing heat to the target fuel [21]. Suzuki and Manzello [21] conclude that lower firebrand fluxes decrease ignition potential, also due to the convective cooling experienced by the target fuel bed during intermitted exposure. This paper proposes that measuring firebrand contact exposure, defined by the quantity of firebrands and the duration of their proximity to fuel, is a useful metric for assessing firebrand ignition potential and will apply this assumption in the results analysis.

Different firebrand contact exposure patterns are observed for all protection configurations for different reference wind speeds tested. As the wind speed increases, the firebrand contact regions are more localised at the windward recirculation zones edges, compared to wider firebrand contact regions spanning the entire windward domain at the lowest wind speed tested. Firebrand contact regions formed at higher wind speeds also involve significantly larger amounts of firebrands compared to the lower reference wind speeds (see Figures 7 and 14). To interpret these distinct particle behaviours the Tachikawa (K) dimensionless number serves to quantify the driving forces influencing the firebrand particles' flight trajectories. The presented simulations consider a lower range of Tachikawa numbers (0.67–2.70) compared to those tested by Nguyen and Kaye [62] in wind tunnel experiments (2.19–6.44) [62]. Nguyen and Kaye found linear relationships between amount of accumulated firebrands on the roof and the inverse Tachikawa number, for a given roof geometry and wind angle. Given this relationship and the lower Tachikawa number range considered in this paper, the expectation is for firebrands to accumulate under all configurations tested; when $K<2$ firebrand contact exposure and the most likely accumulation regions are widespread across the windward floor area, when $K>2$ these accumulation regions concentrate around the wind recirculation zone edges.

Two protection obstacles are tested, a wall and trench protection measure; results show how the introduced protection obstacles divert the firebrand particles trajectories and therefore displace the accumulation location, as well as the firebrand flux received by target cubic structure obstacle. For the particle properties simulated, the trench protection reduced firebrand mass recorded in the immediate surroundings of the cubic structures by 82%–98% depending on the reference wind speed, and the wall protection by 97%–100%. Within the trench protection measure we observe steady increasing accumulation of firebrand particles mass; while windward of wall protection there is transient trajectory of firebrand mass particles, that subsequently change trajectory due to the modified flow field around the structure and are redirected away from the cubic structure. In terms of relative firebrand contact exposure, shown for the two different protection strategies in Figures 10 and 14, all protection strategies redirect firebrand contact exposure further away from the target cubic structure. For the trench protection strategies, the cubic structure is completely protected at 4 m/s from firebrand contact exposure, however windward of the trench protection strategies the firebrand contact trajectories remain the same as the case without protection. At 8 m/s reference wind speed the highest firebrand mass proportion accumulated is within the trench protection. The wall protection-caused reduction in firebrand contact exposure is limited to the expected location of firebrand contact exposure which is moved further windward and away from the target structure.

The simulations presented complement the work by Mankame and Shotorban [15], which investigates firebrand deposition patterns for varying target cuboids structure sizes and aspect ratios at 4.5 m/s reference wind speed; their model considers Lagrangian particle translational and rotational forces, as well as particle temperature and mass loss due to pyrolysis and char oxidation [15]. This work applied a similar methodology, to investigate the influence of surrounding protection strategies and obstacles to quantify the possible reduction in firebrand exposure and the changes in deposition patterns due to varying wind speeds. Aside from differences in the Lagrangian particle model applied, the inlet conditions of particles in the simulation differ in the presented simulations, which apply a vertical particle inlet vent rather than a horizontal one. In both studies particles do not reach the cubic structure's leeward side.

The geometrical simplification in the presented exploratory simulations includes limitations to results accuracy to field conditions. The FDS simulations presented assume an idealised case

10991018, 2025, 5, Downloaded from https://onlinelibrary.wiley.com/doi/10.1002/fam.3286 by Imperial College London, Wiley Online Library on [07/07/2026]. See the Terms and Conditions (https://onlinelibrary.wiley.com/terms-and-conditions) on Wiley Online Library for rules of use; OA articles are governed by the applicable Creative Commons License

without friction between the simulated particles and the solid boundaries; with this assumption the contact between firebrand particles and solid boundaries is maximised, and static particle accumulation is neglected. A conservative firebrand inlet flux scenario is chosen, based on literature values of firebrand generation flux. The distance between the firebrand inlet and the cubic structure is conservatively chosen as close as possible in the domain to allow realistic flow development in the domain, the distance influence on firebrand exposure and protection strategies performance should be characterised. Parametric analysis of wind direction impact on the protection strategies effectiveness is. Wind speed strongly influences the performance of the protection measure. Different wildfire exposure influencing parameters such as distance from fire front and firebrand inlet heights (corresponding to the wildfire flaming front height), need be tested to better characterise the protection measure performance.

5 | Conclusion

This paper explores meaningful parallels between firebrand and sand exposure hazard to infrastructure. To explore the potential applicability of sand hazard protection strategies, exploratory FDS simulations are presented with Lagrangian particles simulating firebrand particles and a wall and trench protection measures windward of a cubic obstacle under three different ambient wind speeds. The simulations show that, in such a simplified scenario, the trench and wall protection methods significantly reduce firebrand exposure to a target obstacle. The firebrand exposure reduction is measured in terms of particles mass within the 25 m^3 surrounding the target cubic structure, resulting in percentage reductions ranging between 82% and 100%. The best reduction is observed with the wall protection at 4 and 8 m/s reference wind speeds, achieving a 100% and 99% reduction respectively, and with the trench protection at 6 m/s, reaching a 98% reduction. Findings offer valuable insights into the design and application of protective strategies to mitigate firebrand flux towards vulnerable buildings or high-risk targets (e.g., storage of flammable substances, power equipment). Parametric studies investigating performance under a wider range of wind speeds, varying wind directions, different protection dimensions need to be conducted to further characterise the strategies' applicability.

Conflicts of Interest

The authors declare no conflicts of interest.

Data Availability Statement

The data that support the findings of this study are available from the corresponding author upon reasonable request.

References

1. S. Meier, R. J. R. Elliott, and E. Strobl, "The Regional Economic Impact of Wildfires: Evidence From Southern Europe," *Journal of Environmental Economics and Management* 118, no. 2022 (2023): 102787, https://doi.org/10.1016/j.jeem.2023.102787.

2. S. L. Manzello, S. Suzuki, M. J. Gollner, and A. C. Fernandez-Pello, "Role of Firebrand Combustion in Large Outdoor Fire Spread," *Progress in Energy and Combustion Science* 76 (2020): 100801, https://doi.org/10.1016/j.pecs.2019.100801.

3. R. Blanchi, J. E. Leonard, and R. H. Leicester, "Lessons Learnt From Post-Bushfire Surveys at the Urban Interface in Australia," *Forest Ecology and Management* 234 (2006): S139, https://doi.org/10.1016/j.foreco.2006.08.184.

4. R. S. P. Hakes, S. E. Caton, D. J. Gorham, and M. J. Gollner, "A Review of Pathways for Building Fire Spread in the Wildland Urban Interface Part II: Response of Components and Systems and Mitigation Strategies in the United States," *Fire Technology* 53, no. 2 (2017): 475–515, https://doi.org/10.1007/s10694-016-0601-7.

5. L. M. Ribeiro, A. Rodrigues, D. Lucas, and D. X. Viegas, "The Impact on Structures of the Pedrógão Grande Fire Complex in June 2017 (Portugal)," *Fire* 3, no. 4 (2020): 1–22, https://doi.org/10.3390/fire3040057.

6. M. Potter and J. Leonard, *Spray System Design for Ember Attack—Research Findings and Discussion Paper* (CSIRO, 2010), 30.

7. S. L. Manzello, "Enabling the Investigation of Structure Vulnerabilities to Wind- Driven Firebrand Showers in Wildland-Urban Interface (WUI) Fires," *Fire Safety Science* 11 (2014): 83–96, https://doi.org/10.3801/IAFSS.FSS.11-83.

8. S. L. Manzello, S.-H. Park, J. R. Shields, Y. Hayashi, and S. Suzuki, "Comparison Testing Protocol for Firebrand Penetration Through Building Vents," in *Summary of BRI/NIST Full Scale and NIST Reduced Scale Results* (NIST, 2010).

9. S. L. Quarles, C. Standohar-Alfano, F. Hedayati, and D. J. Gorham, "Factors Influencing Ember Accumulation Near a Building," *International Journal of Wildland Fire* 32, no. 3 (2023a): 1–8, https://doi.org/10.1071/wf22132.

10. E. Koo, R. R. Linn, P. J. Pagni, and C. B. Edminster, "Modelling Firebrand Transport in Wildfires Using HIGRAD/FIRETEC," *International Journal of Wildland Fire* 21, no. 4 (2012): 396–417, https://doi.org/10.1071/WF09146.

11. E. Koo, P. J. Pagni, D. R. Weise, and J. P. Woycheese, "Firebrands and Spotting Ignition in Large-Scale Fires," *International Journal of Wildland Fire* 19, no. 7 (2010): 818–843, https://doi.org/10.1071/WF07119.

12. A. Wickramasinghe, N. Khan, A. Filkov, and K. Moinuddin, "Physics-Based Modelling for Mapping Firebrand Flux and Heat Load on Structures in the Wildland–Urban Interface," *International Journal of Wildland Fire* 32, no. 11 (2023): 1576–1599, https://doi.org/10.1071/WF22119.

13. S. L. Manzello and S. Suzuki, "Experimentally Simulating Wind Driven Firebrand Showers in Wildland-Urban Interface (WUI) Fires: Overview of the NIST Firebrand Generator (NIST Dragon) Technology," *Procedia Engineering* 62 (2013): 91–102, https://doi.org/10.1016/j.proeng.2013.08.047.

14. R. Wadhwani, D. Sutherland, A. Ooi, K. Moinuddin, and G. Thorpe, "Verification of a Lagrangian Particle Model for Short-Range Firebrand Transport," *Fire Safety Journal* 91, no. May (2017): 776–783, https://doi.org/10.1016/j.firesaf.2017.03.019.

15. A. Mankame and B. Shotorban, "Deposition Characteristics of Firebrands on and Around Rectangular Cubic Structures," *Frontiers in Mechanical Engineering* 7 (2021): 1–14, https://doi.org/10.3389/fmech.2021.640979.

16. S. Suzuki and S. L. Manzello, "Experimental Investigation of Firebrand Accumulation Zones in Front of Obstacles," *Fire Safety Journal* 94 (2017): 1–7, https://doi.org/10.1016/j.firesaf.2017.08.007.

17. S. Suzuki and S. L. Manzello, "Investigating the Effect of Structure to Structure Separation Distance on Firebrand Accumulation," *Frontiers in Mechanical Engineering* 6, no. January (2021a): 1–10, https://doi.org/10.3389/fmech.2020.628510.

18. A. Wickramasinghe, N. Khan, and K. Moinuddin, "Determining Firebrand Generation Rate Using Physics-Based Modelling From

10991018, 2025, 5, Downloaded from https://onlinelibrary.wiley.com/doi/10.1002/fam.3286 by Imperial College London, Wiley Online Library on [07/07/2026]. See the Terms and Conditions (https://onlinelibrary.wiley.com/terms-and-conditions) on Wiley Online Library for rules of use; OA articles are governed by the applicable Creative Commons License

Experimental Studies Through Inverse Analysis," *Fire* 5, no. 1 (2022): 6, https://doi.org/10.3390/fire5010006.

19. B. Y. Lattimer, S. Wong, and J. Hodges, "A Theoretical Model to Understand Some Aspects of Firebrand Pile Burning," *Fire Technology* 58, no. 6 (2022): 3353–3384, https://doi.org/10.1007/s10694-022-01303-5.

20. O. Matvienko, D. Kasymov, E. Loboda, A. Lutsenko, and O. Daneyko, "Modeling of Wood Surface Ignition by Wildland Firebrands," *Fire* 5, no. 2 (2022): 38, https://doi.org/10.3390/fire5020038.

21. S. Suzuki and S. L. Manzello, "Experimental and Theoretical Approaches to Elucidate Fuel Bed Ignition Exposed to Firebrand Showers and Radiant Heat," *International Journal of Heat and Mass Transfer* 202 (2023a): 123740, https://doi.org/10.1016/j.ijheatmasstransfer.2022.123740.

22. L. Zhu and J. L. Urban, "Cooperative Spot Ignition by Idealized Firebrands: Impact of Thermal Interaction in the Fuel," *Fire Safety Journal* 135 2022 (2023): 103701, https://doi.org/10.1016/j.firesaf.2022.103701.

23. P. Intini, E. Ronchi, S. Gwynne, and N. Bénichou, "Guidance on Design and Construction of the Built Environment Against Wildland Urban Interface Fire Hazard: A Review," *Fire Technology* 56 (2020): 1853–1883, https://doi.org/10.1007/s10694-019-00902-z.

24. S. L. Manzello and E. I. D. Foote, "Characterizing Firebrand Exposure From Wildland-Urban Interface (WUI) Fires: Results From the 2007 Angora Fire," *Fire Technology* 50, no. 1 (2014): 105–124, https://doi.org/10.1007/s10694-012-0295-4.

25. J. Hashempour and A. Sharifian, "Effective Factors on the Performance of Woven Wire Screens Against Leaf Firebrand Attacks," *Journal of Fire Sciences* 35, no. 4 (2017): 303–316, https://doi.org/10.1177/0734904117709203.

26. F. Takahashi, "Whole-House Fire Blanket Protection From Wildland-Urban Interface Fires," *Frontiers in Mechanical Engineering* 5 (2019): 60, https://doi.org/10.3389/fmech.2019.00060.

27. S. Suzuki and S. L. Manzello, "Towards Understanding the Effect of Cedar Roof Covering Application on Firebrand Production in Large Outdoor Fires," *Journal of Cleaner Production* 278 (2021b): 123243, https://doi.org/10.1016/j.jclepro.2020.123243.

28. C. Xiong, Y. Liu, C. Xu, and X. Huang, "Acoustical Extinction of Flame on Moving Firebrand for the Fire Protection in Wildland–Urban Interface," *Fire Technology* 57, no. 3 (2021): 1365–1380, https://doi.org/10.1007/s10694-020-01059-w.

29. R. A. Bagnold, *The Physics of Blown Sand and Desert Dunes* (Methuen, 1941), 265.

30. L. Raffaele, N. Coste, and G. Glabeke, "Life-Cycle Performance and Cost Analysis of Sand Mitigation Measures: Toward a Hybrid Experimental-Computational Approach," *Journal of Structural Engineering* 148, no. 7 (2022): 1–14, https://doi.org/10.1061/(asce)st.1943-541x.0003344.

31. L. Raffaele and L. Bruno, "Windblown Sand Action on Civil Structures: Definition and Probabilistic Modelling," *Engineering Structures* 178 (2019): 88–101, https://doi.org/10.1016/j.engstruct.2018.10.017.

32. K. Anusree and G. M. Latha, "Characterization of Sand Particle Morphology: State-of-the-Art," *Bulletin of Engineering Geology and the Environment* 82, no. 7 (2023): 1–30, https://doi.org/10.1007/s10064-023-03309-x.

33. E. Din, *14688-1. Geotechnical Investigation and Testing-Identification and Classification of Soil-Part 1: Identification and Description (ISO 14688-1: 2017), German Version EN ISO* (ISO, 2018), 14681–14688.

34. N. Bouvet and M. Kim, "Firebrands Generated During WUI Fires: A Novel Framework for 3D Morphology Characterization," *Fire Technology* 60, no. 3 (2024): 1503–1542, https://doi.org/10.1007/s10694-023-01530-4.

35. S. Suzuki, S. L. Manzello, M. Lage, and G. Laing, "Firebrand Generation Data Obtained From a Full-Scale Structure Burn," *International Journal of Wildland Fire* 21, no. 8 (2012): 961–968, https://doi.org/10.1071/WF11133.

36. E. P. Cox, "A Method of Assigning Numerical and Percentage Values to the Degree of Roundness of Sand Grains," *Journal of Paleontology* 1, no. 3 (1927): 179–183.

37. F. G. Tickell, "The Examination of Fragmental Rocks," 1947.

38. H. Wadell, "Volume, Shape, and Roundness of Rock Particles," *Journal of Geology* 40, no. 5 (1932): 443–451.

39. T. Zingg, *Beitrag Zur Schotteranalyse* (ETH Zurich, 1935).

40. R. Wadhwani, *Physics-Based Simulation of Short-Range Spotting in Wildfires* (Victoria University, 2019).

41. A. Tohidi, N. Kaye, and W. Bridges, "Statistical Description of Firebrand Size and Shape Distribution From Coniferous Trees for Use in Metropolis Monte Carlo Simulations of Firebrand Flight Distance," *Fire Safety Journal* 77 (2015): 21–35, https://doi.org/10.1016/j.firesaf.2015.07.008.

42. L. Bruno, M. Horvat, and L. Raffaele, "Windblown Sand Along Railway Infrastructures: A Review of Challenges and Mitigation Measures," *Journal of Wind Engineering and Industrial Aerodynamics* 177 (2018): 340–365, https://doi.org/10.1016/j.jweia.2018.04.021.

43. P. Y. Belly, "Sand Movement by Wind, Technical Report," 1964.

44. J. A. Gillies and N. Lancaster, "Large Roughness Element Effects on Sand Transport, Oceano Dunes, California," *Earth Surface Processes and Landforms* 38, no. 8 (2013): 785–792, https://doi.org/10.1002/esp.3317.

45. J. A. Gillies, W. G. Nickling, and J. King, "Aeolian Sediment Transport Through Large Patches of Roughness in the Atmospheric Inertial Sublayer," *Journal of Geophysical Research: Earth Surface* 111, no. 2 (2006): 1–13, https://doi.org/10.1029/2005JF000434.

46. W. T. McLaughlin, "Controlling Coastal Sand Dunes in the Pacific Northwest," 1942.

47. R. D. Tabler, "Design Guidelines for the Control of Blowing and Drifting Snow," 1994.

48. Z. Dong, W. Luo, G. Qian, and H. Wang, "A Wind Tunnel Simulation of the Mean Velocity Fields Behind Upright Porous Fences," *Agricultural and Forest Meteorology* 146, no. 1–2 (2007): 82–93, https://doi.org/10.1016/j.agrformet.2007.05.009.

49. S. Hotta and K. Horikawa, "Function of Sand Fence Placed in Front of Embankment," *Proc. 22nd Conf. Coastal Engineering* (1991): 2754–2767, https://doi.org/10.1061/9780872627765.211.

50. L. Guangyong and M. Peng, "Wind-Preventing Sand-Throwing Wall," 2012.

51. A. Sato and M. Ono, "Snowstorn Guard Fence Structures and Jey Roofs," 1990.

52. K. B. McGrattan, H. R. Baum, R. G. Rehm, A. Hamins, and G. P. Forney, "Fire Dynamics Simulator—Technical Reference Manual," in *NIST Special Publication 1018-1*, vol. 1(5) (US Department of Commerce, National Institute of Standards and Technology, 2021), 175.

53. K. McGrattan, S. Hostikka, R. McDermott, J. Floyd, C. Weinschenk, and K. Overhold, *Fire Dynamics Simulator Technical Reference Guide: Mathematical Model* (NIST Special Publication, 2013), https://doi.org/10.6028/NIST.SP.1018.

54. A. Mankame, P. Damiani, and B. Shotorban, "A Computational Study of the Deposition of Firebrands Between Two Side-by-Side Blocks," *Fire Safety Journal* 150, no. Part A (2024): 104270, https://doi.org/10.1016/j.firesaf.2024.104270. [Correction added on 17 May 2025, after first online publication: Reference 54 has been corrected.].

55. R. Wadhwani, D. Sutherland, A. Ooi, and K. Moinuddin, "Firebrand Transport From a Novel Firebrand Generator: Numerical Simulation of Laboratory Experiments," *International Journal of Wildland Fire* 31, no. 6 (2022): 634–648, https://doi.org/10.1071/WF21088.

10991018, 2025, 5, Downloaded from https://onlinelibrary.wiley.com/doi/10.1002/fam.3286 by Imperial College London, Wiley Online Library on [07/07/2026]. See the Terms and Conditions (https://onlinelibrary.wiley.com/terms-and-conditions) on Wiley Online Library for rules of use; OA articles are governed by the applicable Creative Commons License

56. P. J. Richards and R. P. Hoxey, "Pressures on a Cubic Building—Part 1: Full-Scale Results," *Journal of Wind Engineering and Industrial Aerodynamics* 102 (2012): 72–86, https://doi.org/10.1016/j.jweia.2011.11.004.

57. W. Wegrzynski, T. Lipecki, and G. Krajewski, "Wind and Fire Coupled Modelling—Part II: Good Practice Guidelines," *Fire Technology* 54 (2018): 1443–1485, https://doi.org/10.1007/s10694-018-0749-4.

58. M. El Houssami, E. Mueller, A. Filkov, et al., "Experimental Procedures Characterising Firebrand Generation in Wildland Fires," *Fire Technology* 52, no. 3 (2016): 731–751, https://doi.org/10.1007/s10694-015-0492-z.

59. N. Sardoy, J. L. Consalvi, A. Kaiss, A. C. Fernandez-Pello, and B. Porterie, "Numerical Study of Ground-Level Distribution of Firebrands Generated by Line Fires," *Combustion and Flame* 154, no. 3 (2008): 478–488, https://doi.org/10.1016/j.combustflame.2008.05.006.

60. S. L. Manzello, S. Suzuki, and T. Naruse, "Quantifying Wind-Driven Firebrand Production From Roofing Assembly Combustion," *Fire and Materials* 43, no. 1 (2019): 3–7, https://doi.org/10.1002/fam.2661.

61. D. Nguyen and N. B. Kaye, "The Role of Surrounding Buildings on the Accumulation of Embers on Rooftops During an Ember Storm," *Fire Safety Journal* 131, no. May (2022b): 103624, https://doi.org/10.1016/j.firesaf.2022.103624.

62. D. Nguyen and N. B. Kaye, "Quantification of Ember Accumulation on the Rooftops of Isolated Buildings in an Ember Storm," *Fire Safety Journal* 128, no. 103525 (2022a): 103525, https://doi.org/10.1016/j.firesaf.2022.103525.

63. M. Tachikawa, "A Method for Estimating the Distribution Range of Trajectories of Wind-Borne Missiles," *Journal of Wind Engineering and Industrial Aerodynamics* 29, no. 1–3 (1988): 175–184, https://doi.org/10.1016/0167-6105(88)90156-0.

64. B. Kwon and Y. T. T. Liao, "Effects of Spacing on Flaming and Smoldering Firebrands in Wildland–Urban Interface Fires," *Journal of Fire Sciences* 40, no. 3 (2022): 155–174, https://doi.org/10.1177/07349041221081998.

10991018, 2025, 5, Downloaded from https://onlinelibrary.wiley.com/doi/10.1002/fam.3286 by Imperial College London, Wiley Online Library on [07/07/2026]. See the Terms and Conditions (https://onlinelibrary.wiley.com/terms-and-conditions) on Wiley Online Library for rules of use; OA articles are governed by the applicable Creative Commons License